XLIIIrd RENCONTRES DE MORIOND

Electroweak Interactions and Unified Theories

V - Baryogenesis, Dark matter and Astroparticle Physics

Cross-Reference: indirect dark matter searches are found under
«Neutrino: astrophysics and astroparticle aspects»,
dark matter modes are also considered
in the Standard Model and in the searches sections

QUANTUM BOLTZMANN EQUATIONS IN RESONANT LEPTOGENESIS

A. DE SIMONE
Center for Theoretical Physics, Massachusetts Institute of Technology, Cambridge, MA 02139, USA

The quantum Boltzmann equations relevant for leptogenesis, obtained using non-equilibrium quantum field theory, are described. They manifest memory effects leading to a time-dependent CP asymmetry which depends upon the previous history of the system. This result is particularly relevant in resonant leptogenesis where the asymmetry is generated by the decays of nearly mass-degenerate right-handed neutrinos. The impact of the non-trivial time evolution of the CP asymmetry is discussed either in the generic resonant leptogenesis scenario or in the more specific Minimal Lepton Flavour Violation framework. Significant quantitative differences arise with respect to the usual approach in which the time dependence of the CP asymmetry is neglected.

1 Introduction

In our universe, the difference between the number densities of baryons and anti-baryons, per entropy density, is observed to be [1] $Y_B \equiv (n_B - n_{\bar{B}})/s = (8.84 \pm 0.24) \times 10^{-11}$. This number, obtained from measurements of the Cosmic Microwave Background Radiation, is also in excellent agreement with the independent fit from Big Bang Nucleosynthesis (BBN). Thermal leptogenesis [2] is a simple and well-motivated mechanism to explain this baryon asymmetry. The simplest implementation of this mechanism is realized by adding three right-handed (RH) Majorana neutrinos to the Standard Model (SM), *i.e.* the framework of type I see-saw. The fact that the same see-saw framework may simultaneously account for small neutrino masses and the baryon asymmetry of the universe makes it very attractive. In thermal leptogenesis, the heavy RH neutrinos are produced by thermal scatterings in the early universe after inflation, and subsequently decay out of equilibrium in a lepton number and CP violating way, thus satisfying Sakharov's conditions. A lepton asymmetry then arises, which is partially converted into a baryon asymmetry by electroweak sphaleron interactions.

In the case where the RH neutrinos masses are hierarchical, successful leptogenesis requires the RH neutinos to be heavier than 10^9 GeV. Since they need to be produced after inflation, the reheating temperature cannot be much lower than their mass. In supersymmetric scenarios, this may be in conflict with the upper bound on the reheating temperature necessary to avoid the overproduction of gravitinos during rehating, which may spoil the successful predictions of BBN. On the other hand, if the RH neutrinos are nearly degenerate in mass, the self-energy contribution to the CP asymmetries may be resonantly enhanced, thus making leptogenesis viable at temperatures as low as TeV. This interesting situation is called "resonant leptogenesis" [3].

In order to precisely quantify the lepton asymmetry generated by the leptogenesis mechanism, one needs to keep track of the abundances of the particles involved in the process by solving a set of coupled Boltzmann equations. The standard calculations employ a set of semi-classical equations. However, quantum Boltzmann equations for leptogenesis have been recently derived [4] (for an earlier study, see Ref. [5]), using a Green's function technique known as Closed Time-Path (CTP) — or Schwinger-Keldysh — formalism [6], which provides a complete description of non-equilibrium phenomena in field theory. While in the semi-classical setup every scattering in the plasma is independent of the previous one, in a full quantum approach the whole dynamical history of the system is taken into account. The quantum Boltzmann equations describe therefore a non-Markovian dynamics, manifesting the typical "memory" effects which are observed in quantum transport theory [7]. The thermalization rate obtained from the quantum transport theory may be substantially longer than the one obtained from the classical kinetic theory.

Furthermore, and more importantly, the CP asymmetry turns out to be a function of time, even after taking the Markovian limit. Its value at a given instant depends upon the previous history of the system. If the timescale of the variation of the CP asymmetry is shorter than the relaxation time of the particles abundances, the CP asymmetry may be averaged over many scatterings and it reduces to its classical constant value; the solutions to the quantum and the classical Boltzmann equations are expected to differ only by terms of the order of the ratio of the timescale of the CP asymmetry and the relaxation timescale of the particle distributions. In thermal leptogenesis with hierarchical RH neutrinos this is typically the case. However, in the resonant leptogenesis scenario, where at least two RH neutrinos are almost degenerate in mass and their mass difference ΔM is of the order of their decay rates, the typical timescale to build up coherently the CP asymmetry (of the order of $1/\Delta M$) can be larger than the timescale for the change of the abundance of the RH neutrinos. Thus, in the case of resonant leptogenesis significant differences are expected between the classical and the quantum approach.

2 Quantum Boltzmann equations

The model I consider consists of the SM plus three RH neutrinos N_i ($i = 1, 2, 3$), with Majorana masses $M_1 \leq M_2 \leq M_3$. The interactions among RH neutrinos, Higgs doublets H, lepton doublets ℓ_α and singlets e_α ($\alpha = e, \mu, \tau$) are described by the Lagrangian

$$\mathscr{L}_{\rm int} = \lambda_{i\alpha}\, N_i\, \ell_\alpha\, H + h_\alpha\, \bar{e}_\alpha\, \ell_\alpha\, H^c + \frac{1}{2} M_i N_i^2 + \text{h.c.}\,, \tag{1}$$

with summation over repeated indices. In the early universe, the quantum numbers conserved by sphaleron interactions are $\Delta_\alpha = B/3 - L_\alpha$, where B, L_α are the baryon asymmetry and the lepton asymmetry in the flavour α, respectively.

The quantum Boltzmann equations describing the generation of the baryon asymmetry are obtained using the CTP formulation of non-equilibrium quantum field theory. The reader is referred to Ref. [4] for the technical details of the calculation. Here, I only summarize the main results. After taking the Markovian limit, the equations for the number densities of RH neutrinos

Y_{N_i} and the asymmetries Y_{Δ_α} (per entropy density) read

$$\frac{dY_{N_i}}{dz} = -D_i \left(Y_{N_i} - Y_{N_i}^{\rm eq}\right), \tag{2}$$

$$\frac{dY_{\Delta_\alpha}}{dz} = -\sum_i \epsilon_{i\alpha} D_i \left(Y_{N_i} - Y_{N_i}^{\rm eq}\right) - W_\alpha |A_{\alpha\alpha}| Y_{\Delta_\alpha}, \tag{3}$$

where the ratio between the mass of the lightest RH neutrino and the temperature $z = M_1/T$ plays the role of the time variable. At equilibrium the N_i number density normalized to the entropy density of the universe is given by $Y_{N_i}^{\rm eq} = z_i^2 \mathcal{K}_2(z_i)/(4g_*)$, where $z_i = z\sqrt{x_i}$, $x_i = (M_i/M_1)^2$, $g_* = 106.75$ and $\mathcal{K}_n(z_i)$ is a modified Bessel function of the n-th kind. The decay and washout terms appearing in (2)-(3) are defined as

$$D_i = K_i \; x_i \; z \; \frac{\mathcal{K}_1(z_i)}{\mathcal{K}_2(z_i)}, \qquad W_\alpha = \sum_i \frac{1}{4} K_{i\alpha} \; \sqrt{x_i} \; \mathcal{K}_1(z_i) \; z_i^3, \tag{4}$$

where the washout parameters are given by the ratios between the decay rates and the Hubble parameter

$$K_{i\alpha} = \frac{\Gamma(N_i \to \ell_\alpha \bar{H})}{H(T = M_i)}, \qquad K_i = \sum_\alpha K_{i\alpha}. \tag{5}$$

The form of the matrix A depends on the number of lepton flavours which are effective in the dynamics of leptogenesis, and this in turn depends on the temperature at which leptogenesis takes place, which is roughly given by M_1. Indeed, for $M_1 \gtrsim 10^{12}$ GeV all lepton flavours are not distinguishable and the one-flavour regime holds; for $10^9 {\rm GeV} \lesssim M_1 \lesssim 10^{12} {\rm GeV}$ and $M_1 \lesssim 10^9$ GeV, two and three lepton flavours become effective, respectively [8,9]. For example, in the approximation where A is a diagonal matrix $A = -{\rm diag}(151/179, 344/537, 344/537)$, for $M_1 \lesssim 10^9 {\rm GeV}$. The complete expressions can be found in Refs.[8]. Finally, sphaleron interactions introduce a conversion factor for the final baryon asymmetry

$$Y_B = \frac{12}{37} \sum_\alpha Y_{\Delta_\alpha}(z \to \infty). \tag{6}$$

The key quantities controlling the production of a net lepton number are the CP asymmetries in the N_i decays

$$\epsilon_{i\alpha} \equiv \frac{\Gamma(N_i \to \ell_\alpha \bar{H}) - \Gamma(N_i \to \bar{\ell}_\alpha H)}{\Gamma(N_i \to \ell_\alpha \bar{H}) + \Gamma(N_i \to \bar{\ell}_\alpha H)}. \tag{7}$$

The Eqs. (2)-(3) reproduce exactly the usual Boltzmann equations obtained in the semiclassical approach, except for a crucial difference in the source term of (3). As mentioned above, the inclusion of quantum effects introduces a time dependence in the CP asymmetry

$$\epsilon_{i\alpha}(z) = \sum_{j \neq i} \epsilon_\alpha^{(j,i)} \, m^{(i,j)}(z), \tag{8}$$

$$m^{(i,j)}(z) = 2 \; \sin^2\left(\frac{1}{2}\frac{M_j - M_i}{2H(M_1)} z^2\right) - \frac{\Gamma_j}{M_j - M_i} \; \sin\left(\frac{M_j - M_i}{2H(M_1)} z^2\right), \tag{9}$$

$$\epsilon_\alpha^{(j,i)} = \frac{1}{8\pi} \frac{{\rm Im}\left[\lambda_{i\alpha}\lambda_{\alpha j}^\dagger (\lambda\lambda^\dagger)_{ij}\right]}{(\lambda\lambda^\dagger)_{ii}} \; (g_s^{(j,i)} + g_v^{(j,i)}), \tag{10}$$

$$g_s^{(j,i)} = \sqrt{\frac{x_j}{x_i}} \; \frac{1}{1 - \frac{x_j}{x_i}} \; \frac{1}{1 + \frac{\Gamma_j^2/M_i^2}{(1 - x_j/x_i)^2}}, \tag{11}$$

$$g_v^{(j,i)} = \sqrt{\frac{x_j}{x_i}} \; \left(1 - (1 + \frac{x_j}{x_i}) \; \ln\frac{1 + x_j/x_i}{x_j/x_i}\right), \tag{12}$$

where $\Gamma_j \equiv \sum_\beta \Gamma(N_j \to \ell_\beta \bar{H}) = (\lambda\lambda^\dagger)_{jj} M_j/(8\pi)$ is the total decay rate of the j-th RH neutrino, g_s and g_v are the self-energy and the vertex correction functions, respectively.

In the quantum approach, the typical timescale for the variation of the CP asymmetry is

$$t = \frac{1}{2H(T)} = \frac{z^2}{2H(M_1)} \sim \frac{1}{M_j - M_i} = \frac{1}{\Delta M_{ji}} \,. \tag{13}$$

If the timescale for the variation of the particle abundances $1/\Gamma_i$ is much larger than $1/\Delta M_{ji}$, the CP asymmetry will average to its classical value $\bar{\epsilon}_{i\alpha} = \sum_{j\neq i} \epsilon_\alpha^{(j,i)}$ and no significant quantum effect arises. On the other hand, quantum effects are expected to be sizeable if the timescale $1/\Delta M_{ji}$ for building up coherently the CP asymmetry is larger than the timescale $1/\Gamma_i$ for changing the abundances. In other words, the oscillation frequency ΔM_{ji} has to be sufficiently smaller than Γ_i, so that the factors $m^{(i,j)}(z)$ do not effectively average to one. Under these conditions, the amplitude of the "sin" term in $m^{(i,j)}(z)$ is also enhanced, which turns out to be a crucial effect.

The above discussion allows one to formulate a quantitative criterion for the importance of quantum effects, namely $\Delta M_{ji} \lesssim \Gamma_i$. This criterion can be naturally satisfied if RH neutrinos are nearly degenerate, such as in resonant leptogenesis and in models based on Minimal Lepton Flavour Violation.

3 Application to resonant leptogenesis

As anticipated in the Introduction, resonant leptogenesis relies on the fact that the CP asymmetries are resonantly enhanced when the mass differences among RH neutrinos are comparable to their decay widths. $\Delta M_{ij} \sim \Gamma_i \sim \Gamma_j$. Therefore, the criterion for the significance of the quantum effects is satisfied and one expects the quantum Boltzmann equations to provide appreciably different results with respect to their semi-classical counterparts.

For the sake of simplicity, let us restrict here to the simplest case where there are only two RH neutrinos with mass difference ΔM and similar decay rates Γ_N, in the one-flavour approximation where α has a single value. In this case, the Boltzmann equation for the lepton asymmetry in the single flavour α contains the CP asymmetry

$$\epsilon_\alpha(z) \simeq \bar{\epsilon}_\alpha \left[2 \sin^2 \left(\frac{K z^2}{4} \frac{\Delta M}{\Gamma_N} \right) - \frac{\Gamma_N}{\Delta M} \sin \left(\frac{K z^2}{2} \frac{\Delta M}{\Gamma_N} \right) \right] , \tag{14}$$

where $\bar{\epsilon}_\alpha = \sum_i \sum_{j\neq i} \epsilon_\alpha^{(j,i)}$ is the constant value of the asymmetry in the classical limit, and K is the total washout parameter.

The plot in Fig. 1 shows the absolute values of the final lepton asymmetry computed with and without the time-dependent factor in (14). For the strong washout regime $K \gtrsim 1$, the quantum and semi-classical methods give almost the same answers; instead, at small K, the discrepancy between the two approaches is sizeable, of an order of magnitude or more. This is easily understood from Eq. (14), where at large K the "sin" functions average to constants while in the opposite case they determine an appreciable time-dependence of the CP asymmetry.

In Ref. [10], the reader can find a more detailed study of the more general "flavoured" case as well as analytical approximations for the lepton asymmetries in the different possible washout regimes. They reproduce fairly well the numerical solutions of the Boltzmann equations (2)-(3).

3.1 MLFV leptogenesis

Nearly degenerate RH neutrinos naturally arise in the context of models satisfying the hypothesis of Minimal Flavour Violation (MFV) [11,12]. In the quark sector, where the MFV hypothesis has

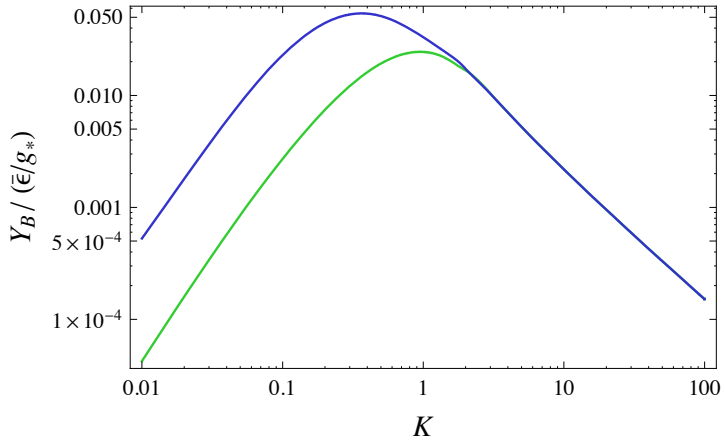

Figure 1: The absolute value of the final baryon asymmetry, as a function of K, for $\Delta M = \Gamma_N$. In blue, the time dependence in the CP asymmetry is included; in green, the usual time-independent CP asymmetry is used.

been formulated first, the MFV ansatz states that the two quark Yukawa couplings are the only irreducible breaking sources of the flavour-symmetry group defined by the gauge-kinetic lagrangian [11]. In generic models satisfying this hypothesis, quark Flavour Changing Neutral Currents are naturally suppressed to a level comparable to experiments and new degrees of freedom can naturally appear in the TeV range. The extension of the MFV hypothesis to the lepton sector (MLFV) has been formulated in Ref. [12], where a number of possible scenarios, depending on the field content of the theory, have been identified. The case more similar to the quark sector and more interesting from the point of view of leptogenesis is the so-called extended field content scenario. The lepton field content is extended by three heavy RH neutrinos with degenerate masses at the tree level. The largest lepton flavour symmetry group of the gauge-kinetic term is $SU(3)_\ell \otimes SU(3)_e \otimes O(3)_N$ and, according to the MLFV hypothesis, it is assumed that this group is broken only by the charged-lepton and neutrino Yukawa couplings h_α and $\lambda_{i\alpha}$. In relation to leptogenesis, the key feature of this scenario is that the degeneracy of the RH neutrinos is lifted only by corrections induced by the Yukawa couplings, so that we end up with a highly constrained version of resonant leptogenesis.

Within this setup, the viability of leptogenesis has been considered either in the one-flavour approximation [13] or in the flavoured case [14]. However, in the light of the quantum version of the Boltzmann equations I discussed here, it turned out necessary to carry out an analysis to assess the impact of the quantum effect in this MLFV leptogenesis scenario. It has been shown in [15], both analytically and numerically, that neglecting the time dependence of the CP asymmetry may underestimate the baryon asymmetry by several orders of magnitude when a strong degeneracy among heavy RH neutrinos and small mass splittings in the light neutrino sectors are present. This is true both when the CP phases come from the RH sector and when they come entirely from the left-handed sector and may be identified with the low energy PMNS phases.

4 Conclusions

The simplest see-saw framework, where RH neutrinos are added to the particle content of the SM, may simultaneously account for the small neutrino masses and the baryon asymmetry of the universe, through the leptogenesis mechanism. Obtaining detailed results in leptogenesis requires solving the Boltzmann equations for the abundances of the particles involved. In this talk, I have presented a set of quantum Boltzmann equations which has been derived using non-

equilibrium quantum field theory. The main difference with respect to the usual semi-classical equations is that the CP asymmetry is time-dependent. A criterion to discriminate situations where one should expect quantum effects to be important has been discussed. In particular, this condition is satisfied in realistic models such as resonant and MLFV leptogenesis. In these scenarios, quantum effects play a significant role and should be taken into account.

Acknowledgments

I am grateful to the organizers for their kind invitation. This contribution is based on work done in collaboration with A. Riotto and with V. Cirigliano, G. Isidori, I. Masina. I acknowledge support from the INFN "Bruno Rossi" Fellowship, from the U.S. Department of Energy (DoE) under contract No. DE-FG02-05ER41360, and from an EU Marie Curie Grant.

References

1. J. Dunkley *et al.* [WMAP Collaboration], arXiv:0803.0586 [astro-ph].
2. M. Fukugita and T. Yanagida, Phys. Lett. B **174**, 45 (1986); M. A. Luty, Phys. Rev. D **45**, 455 (1992). G. F. Giudice, A. Notari, M. Raidal, A. Riotto and A. Strumia, Nucl. Phys. B **685**, 89 (2004) [arXiv:hep-ph/0310123]; W. Buchmuller, P. Di Bari and M. Plumacher, Annals Phys. **315** (2005) 305 [arXiv:hep-ph/0401240]. For a recent comprehensive review, see: S. Davidson, E. Nardi and Y. Nir, arXiv:0802.2962 [hep-ph].
3. A. Pilaftsis and T. E. J. Underwood, Nucl. Phys. B **692**, 303 (2004) [arXiv:hep-ph/0309342]; A. Pilaftsis and T. E. J. Underwood, Phys. Rev. D **72**, 113001 (2005) [arXiv:hep-ph/0506107];
4. A. De Simone and A. Riotto, JCAP **0708** (2007) 002 [arXiv:hep-ph/0703175].
5. W. Buchmuller and S. Fredenhagen, Phys. Lett. B **483**, 217 (2000) [arXiv:hep-ph/0004145].
6. For a review, see: K. Chou, Z. Su, B. Hao and L. Yu, Phys. Rep. **118** 1, (1985).
7. P. Danielewicz, Annals Phys. **152**, 239 (1984); P. Danielewicz, Annals Phys. **152**, 305 (1984); P.A. Henning, Phys. Rep. **253**, 235 (1995).
8. R. Barbieri, P. Creminelli, A. Strumia and N. Tetradis, Nucl. Phys. B **575** (2000) 61; T. Endoh, T. Morozumi and Z. h. Xiong, Prog. Theor. Phys. **111** (2004) 123; A. Abada, S. Davidson, F. X. Josse-Michaux, M. Losada and A. Riotto, JCAP **0604**, 004 (2006); E. Nardi, Y. Nir, E. Roulet and J. Racker, JHEP **0601**, 164 (2006); A. Abada, S. Davidson, A. Ibarra, F. X. Josse-Michaux, M. Losada and A. Riotto, JHEP **0609**, 010 (2006).
9. A. De Simone and A. Riotto, JCAP **0702** (2007) 005 [arXiv:hep-ph/0611357].
10. A. De Simone and A. Riotto, JCAP **0708** (2007) 013 [arXiv:0705.2183 [hep-ph]].
11. G. D'Ambrosio, G. F. Giudice, G. Isidori and A. Strumia, Nucl. Phys. B **645** (2002) 155 [arXiv:hep-ph/0207036].
12. V. Cirigliano, B. Grinstein, G. Isidori and M. B. Wise, Nucl. Phys. B **728** (2005) 121 [arXiv:hep-ph/0507001].
13. V. Cirigliano, G. Isidori and V. Porretti, Nucl. Phys. B **763** (2007) 228 [arXiv:hep-ph/0607068].
14. G. C. Branco, A. J. Buras, S. Jager, S. Uhlig and A. Weiler, JHEP **0709** (2007) 004 [arXiv:hep-ph/0609067]; S. Uhlig, JHEP **0711** (2007) 066 [arXiv:hep-ph/0612262].
15. V. Cirigliano, A. De Simone, G. Isidori, I. Masina and A. Riotto, JCAP **0801** (2008) 004 [arXiv:0711.0778 [hep-ph]].

THE CRESST-II EXPERIMENT

RAFAEL F. LANG
Max-Planck-Institut für Physik, Föhringer Ring 6, D-80805 München, Germany,
E-mail rafael@cresst.de

For the CRESST Collaboration: G. Angloher, M. Bauer, I. Bavykina, A. Bento, A. Brown, C. Bucci, C. Ciemniak, C. Coppi, G. Deuter, F. von Feilitzsch, D. Hauff, S. Henry, P. Huff, J. Imber, S. Ingleby, C. Isaila, J. Jochum, M. Kiefer, M. Kimmerle, H. Kraus, J. Lanfranchi, R. F. Lang, M. Malek, R. McGowan, V. B. Mikhailik, E. Pantic, F. Petricca, S. Pfister, W. Potzel, F. Pröbst, S. Roth, K. Rottler, C. Sailer, K. Schäffner, J. Schmaler, S. Scholl, W. Seidel, M. Stark, L. Stodolsky, A. J. B. Tolhurst, I. Usherov, W. Westphal.

The CRESST-II experiment in the Laboratori Nazionali del Gran Sasso uses scintillating crystals as a target to search for elastic scatterings of dark matter particles in a laboratory environment. The detectors are operated in a dilution cryostat at temperatures below 30 mK, and for each particle interaction, the phonon signal as well as the scintillation light signal are recorded. The current limit that can be placed on the spin-independent WIMP-nucleon scattering cross-section with this technique is below 6×10^{-7} pb for WIMPs in the mass range from about 40 to 90 GeV/c^2.

1 Introduction

It remains one of the most pressing problems of physics today to clarify the nature of dark matter. So far, the evidence for a significant component of non-baryonic dark matter in the universe is compelling. It stems from a variety of independent experiments, ranging from measurements of the cosmic microwave background [1] and big bang nucleosynthesis [2] to astrophysical observations of large amounts of unseen matter in galaxy clusters [3] and galaxies [4]. Yet, the nature of this component is still unknown, so experiments to unravel this mystery are more important than ever.

Highly motivated candidates for dark matter are weakly interacting, yet massive particles (WIMPs) [5]. These particles are expected to be gravitationally bound in the Milky Way in a roughly isothermal halo, thus following a Maxwell-Boltzmann-distribution [6,7]. The WIMP density at the position of the Earth is assumed to be around 0.3 GeV/cm^3. On our way around

the Galaxy we pass through this halo with a velocity of about 220 km/s, and we hope to detect the scattering of this WIMP wind on nuclei in an absorber.

Accelerator searches for new forms of matter place a lower bound on the mass of these particles of the order of 10 GeV/c^2. Since the de Broglie wavelength of particles with such mass and velocity is larger than the radius of a nucleus, one may expect the scattering to occur in a coherent way, the case we consider here. Then, for a given target material with mass number A, the scattering amplitude scales as A^2, favoring heavy nuclei for a search experiment.

2 Scintillating Crystals

Following the interaction of a WIMP with a target nucleus, the energy of the recoil is very small, typically only of the order of 10 keV. Together with the very small expected interaction rate of less than 10 events per kilogram of target and year of measuring time, available technologies are highly constrained. So the two main requirements to this kind of experiment are a very low energy threshold and the capability to reject backgrounds caused by known particle species.

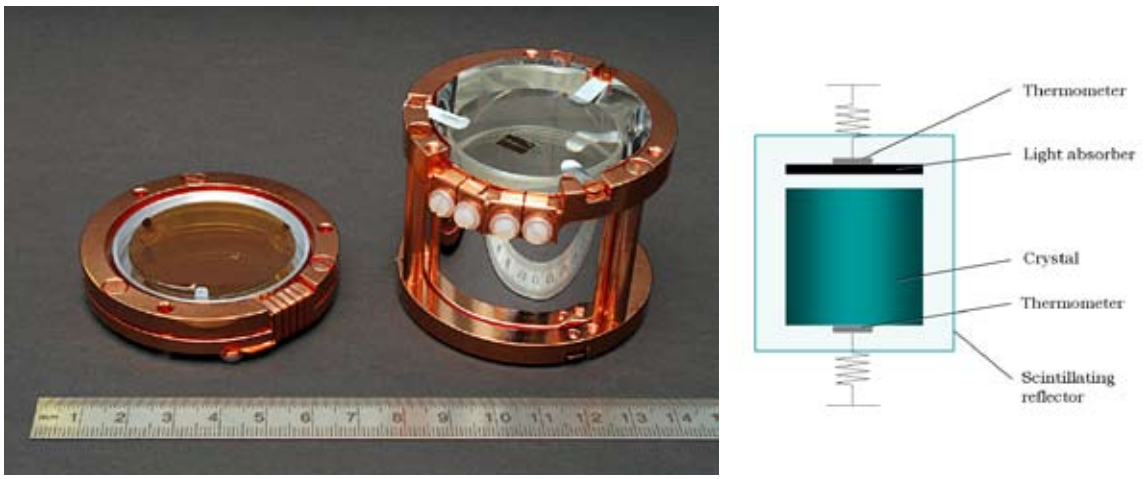

Figure 1: A detector module as used in the CRESST-II experiment. Left picture: An open module with the light absorbing wafer on the left hand side and the scintillating crystal in its housing on the right hand side. Sketch: a tungsten superconducting phase transition thermometer is evaporated onto a $CaWO_4$ target crystal. A second thermometer is evaporated on a light absorber to measure the scintillation light. Both detectors are enclosed in a scintillating reflective housing.

In the second phase of the Cryogenic Rare Event Search with Superconducting Thermometers CRESST-II [8] we use scintillating crystals as target material [9]. They are shaped as cylinders of (4×4) cm and weigh about 300 g each. We operate them as calorimeters at temperatures as low as 10 mK. In such dielectric crystals, most of the energy of a particle interaction goes into phonons. To measure these phonons, we evaporate a thin tungsten film onto the crystal. Tungsten becomes superconducting in this temperature range, and stabilizing the film in its superconducting phase transition (by means of a dedicated heater) makes an extremely sensitive thermometer: Any particle interaction warms up the film, thus changing its resistance, which can be measured with sensitive electronics [10].

In addition to this phonon signal, a small fraction of the interaction energy (typically a few percent) is emitted as scintillation light. To detect this light, we use another tungsten phase transition thermometer on a separate light absorbing wafer. Thus, for each target crystal, we have two thermometers, one measuring the deposited energy, and the other measuring the scintillation light, see figure 1.

We define the *light yield* of an interaction as the amount of energy in the light detector divided by the energy in the phonon detector, and normalize it such that electron recoils have

a light yield of 1. Electron recoils are caused by electrons and gammas that impinge onto the crystal. Compared to such events, the light yield of alpha particles is reduced by a factor of 5. Neutrons are mainly seen when they scatter from oxygen due to the kinematics of the interaction, with a light yield reduced by a factor of 10 relative to that of the electron recoils. Coherent scatterings of WIMPs are expected to take place mainly on tungsten where the light yield is reduced by a factor of 40 [11]. Thus, simultaneously measuring the light signal allows us to discriminate the (possibly WIMP induced) tungsten recoils from the dominant radioactive backgrounds.

3 The Upgraded Setup

In 2007, the experimental setup was extended to be capable of housing up to 33 detector modules. To shield them as much as possible from ambient radioactivity, we provide a variety of shielding layers. The experiment is hosted in the Laboratori Nazionali del Gran Sasso, Italy, to shield the detectors from cosmic ray induced backgrounds with the overburden of 1400 m of rock. During the upgrade, we added a muon veto to discriminate residual muon induced backgrounds, as well as a 45 cm thick wall of polyethylene to moderate neutrons to energies below detection threshold. The setup is constantly flushed with nitrogen vapor, in particular to keep radon contaminated air away from the inner parts. A 20 cm thick lead shield and a 14 cm copper shield absorb gamma radiation coming from outside. Also, the fivefold thermal shielding of the cryostat provides an additional 1.2 cm thick copper shield. All the materials in the vicinity of the detectors are selected for radiopurity and handled in a clean room environment.

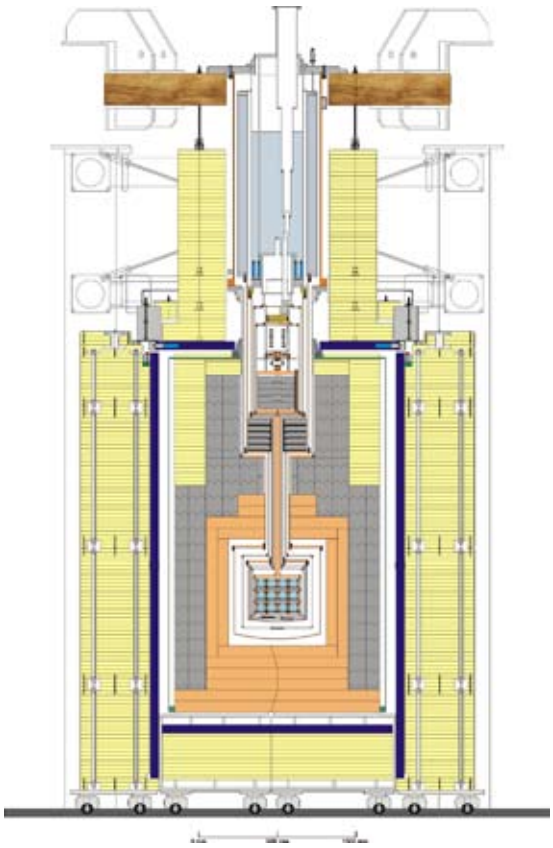

Figure 2: Setup of CRESST-II. The detectors are in a low-background environment in the center of the shielding. The cryostat (upper part of the figure) is kept away from this very clean environment. The polyethylene neutron shield is shown in yellow, the lead shield in gray, and the copper shield in orange. A muon veto made from plastic scintillator, shown in blue, helps to further reduce backgrounds induced by cosmic rays.

4 Results

After a major upgrade [12] we installed 10 detector modules and cooled the cryostat for commissioning of the new setup. The detectors were calibrated with a gamma source to set the energy scale, as well as a neutron source for validation of the light yield anticipated for nuclear recoils. The data reported here was taken in 2007 with two detector modules from March 27th through July 23rd.

We fit the pulses using a template fit, which is constructed from pulses from the gamma calibrations. In order to treat noise in an unbiased way, we allow the amplitude of the fit to take negative values. This guarantees that for no signal, the reconstructed amplitudes indeed scatter around zero with a width corresponding to the noise. Thus negative amplitudes can arise, resulting in events with negative light yields.

We perform only very basic quality cuts on the data, rejecting pulses only if they occur in one of the rare periods when the temperature of the cryostat is not as stable as desired, if they are direct hits of the light detector or the thermometer on the crystal, or if they are pile-up events. Events recorded from the two detectors with a cumulative exposure of 50 kg d are shown as scatter plot in figure 3.

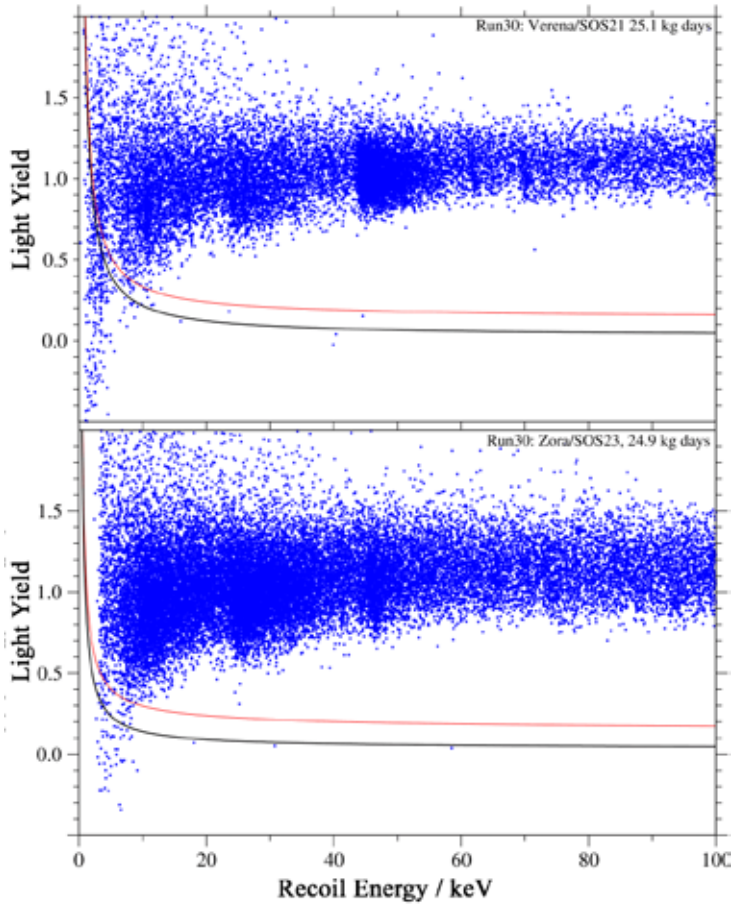

Figure 3: Low energy event distribution measured with two 300 g $CaWO_4$ detector modules during the commissioning run in 2007. The vertical axis represents the light yield expressed as the ratio (energy from the light channel)/(energy from the phonon channel), the horizontal axis is the total energy measured by the phonon channel. Below the red curve we expect 90% of all nuclear recoils, and below the black curve 90% of the tungsten recoils. The acceptance window is set below the black line and between 11 keV (above which we can discriminate electron recoils) and 40 keV (below which most of the WIMP induced recoils appear).

5 Discussion

To derive a limit on the coherent WIMP-nucleus scattering cross section, standard assumptions on the dark matter halo [6,7] are adopted. The finite extension of the nuclei is taken into account by assuming the Helm form factor [13], which basically limits the energy transfer to the tungsten nuclei to energies below 40 keV for all WIMP masses. In the energy region above 11 keV, where recoil discrimination becomes efficient, to up to 40 keV, 4 tungsten recoil events were observed in the data of figure 3. Combining this data with data from the previous run [9], the upper limit for the WIMP scattering cross-section per nucleon is set using Yellin's optimum interval method [14], shown as the red curve in figure 4. The minimum of this curve is below 6×10^{-7} pb for WIMPs with masses between 40 and 90 GeV/c^2, obtained after a gross exposure (including down times due to refilling of cryogenic liquids etc.) of only 67 kg d.

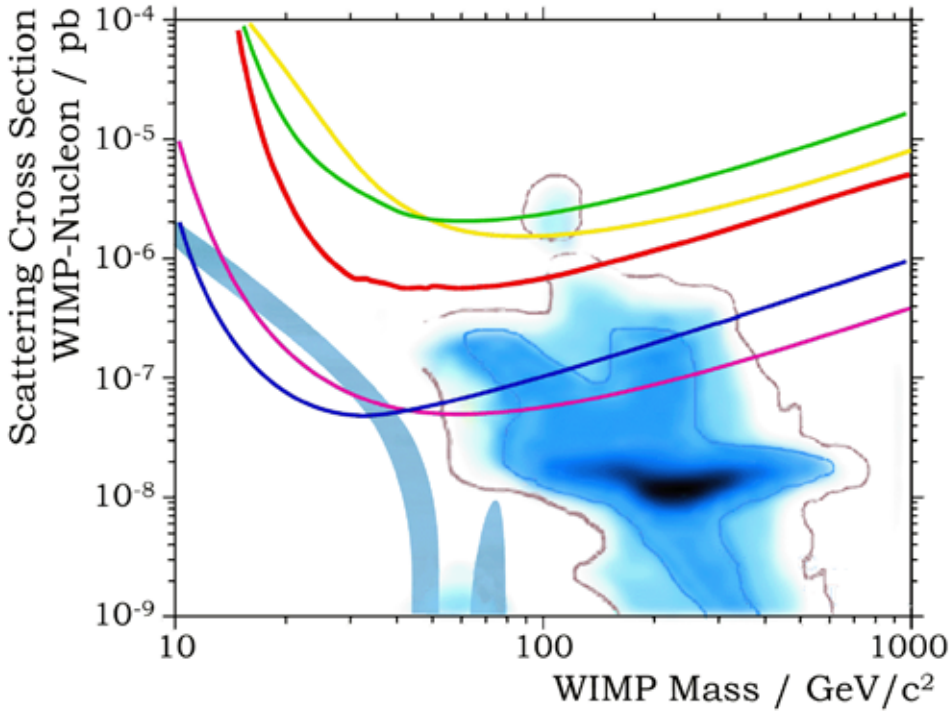

Figure 4: Exclusion limits on the WIMP-nucleon spin independent scattering cross section from a few experiments, from top to bottom from the KIMS experiment (green), EDELWEISS (yellow), XENON10 (blue) and CDMS (violet). The red curve is the limit from the CRESST experiment, derived from the data of figure 3 and that of the previous run. In cyan two theoretical expectations.

The few events that we observe in our signal area need not be WIMP induced tungsten recoil events. During the commissioning, a weak point in the neutron shielding above the muon veto was identified, but patched only after data taking was completed. This background can be estimated to account for the observed number of events in the nucleon recoil band. In addition we might have a small neutron background induced by decays from radioactive contaminations in the other crystals that were not running during this data taking period, a situation unique to this commissioning phase. The upcoming run should clarify on these points.

In the hunt for a discovery one might want to compare the different technologies, and since exclusion limits are one way of doing so, figure 4 also shows the results from a few other experiments: From the KIMS experiment [15] using a gross exposure of 3409 kg d on CsI(Tl), the EDELWEISS experiment [16] ($\approx$ 180 kg d, Ge), XENON10 [17] (1980 kg d, Xe) and CDMS [18] ($\approx$ 1250 kg d, Ge). The figure also contains two expectations from theory [19,20].

References

1. G. Hinshaw et al., ApJ. Supp. *to be published* (2008), arXiv:0803.0732.
2. G. Steigman, Ann. Rev. Nuc. Part. Sci. **57** (2007) 463–491, arXiv:0712.1100.
3. D. Clowe et al., ApJL. **648** (2007) L109–L113, arXiv:astro-ph/0608407.
4. X.-X. Xue et al., ApJ. *to be published* (2008), arXiv:0801.1232.
5. G. Jungman et al., Phys. Rep. **267** (1996) 195–373, arXiv:hep-ph/9506380.
6. F. Donato, N. Fornengo and S. Scopel, Astropart. Phys. **9** (1998) 247–260, arXiv:hep-ph/9803295.
7. J. D. Lewin and P. F. Smith, Astropart. Phys. **6** (1996) 87–112.
8. G. Angloher et al., Astropart. Phys. **18**, 43–55 (2002).
9. G. Angloher et al., Astropart. Phys. **23**, 325–339 (2005).
10. S. Henry et al., J. Inst. **2** (2007) P11003.
11. J. Ninkovic et al., NIM A **564** (2006) 567–578, arXiv:astro-ph/0604094.
12. G. Angloher et al., *to be published* (2008).
13. R. H. Helm, Phys. Rev. **104** (1956) 1466–1475.
14. S. Yellin, Phys. Rev. D **66** (2002) 032005, arXiv:physics/0203002.
15. H. S. Lee et al., PRL **99** (2007) 091301, arXiv:0704.0423.
16. V. Sanglard et al., Phys.Rev. D **71** (2005) 122002, arXiv:astro-ph/0503265.
17. J. Angle et al., PRL **100** (2008) 021303, arXiv:0706.0039.
18. Z. Ahmed et al., *submitted to PRL* (2008), arXiv:0802.3530.
19. C. P. Burgess, M. Pospelov and T. ter Veldhuis, Nucl. Phys. B **619** (2001) 709-728, arXiv:hep-ph/0011335.
20. L. Roszkowski, R. R. de Austri and R. Trotta, JHEP **07** (2007) 075, arXiv:0705.2012.

Recent results in very high energy gamma ray astronomy

J-F. GLICENSTEIN
DSM/IRFU/SPP
CEA-Saclay, F-91191 Gif-sur-Yvette, France

The very high energy (E ¿50 GeV) gamma ray astronomy is an emerging field. Three major Imaging Atmospheric Cherenkov Telescope collaborations, HESS, MAGIC and VERITAS are presently in operation.Many new results in astroparticle physics have been obtained by these instruments. In this paper, Galactic Center observations, dark matter searches and limits on Lorentz invariance violation are reported.

1 Introduction

The very high energy (VHE) gamma ray astronomy is a new emerging field. This paper focuses on selected results from the VHE gamma ray instruments which are of interest to the particle physics community. The first section reviews the experimental status. Next, recent results on the Galactic Centre from the HESS collaboration are reported. These results constrain the source of the VHE gamma ray emission. The next section is dedicated to indirect dark matter searches.More than 15 Active Galactic Nuclei (AGN) have been observed in the TeV regime. These distant variable sources allow to test for Lorentz invariance breaking. The final section reports constraints on violations of the Lorentz invariance obtained by the MAGIC collaboration.

2 The very high energy gamma ray instruments

Ground based very high energy gamma ray instruments detect atmospheric cascades initiated by astrophysical gamma-rays. These intruments are sensitive to photons in the range 50 GeV to 100 TeV. The two major classes of instruments are imaging atmospheric Cherenkov telescopes (IACT) and shower particle detectors. The characterictics of major currently operating IACTs are summarized in table 1. These instruments are the HESS, VERITAS and CANGAROO-III arrays and the MAGIC telescope. Each of their telescope is equipped with a finely pixelized camera at its focus. A large fraction of the cosmic ray background is rejected with the analysis of the Cherenkov image. In addition,Cherenkov arrays use stereoscopy to improve their background rejection and their energy/angular resolution.

Table 1: Principal caracteristics of currently operating major IACTs

Instrument	lat. (deg)	long (deg)	Altitude (m)	Tels	Telescope Area (m^2)	Camera Pixels	FOV (deg)	Threshold (TeV)
HESS	-23	16	1800	4	107	960	5	0.1
MAGIC	29	18	2225	1	234	574	3.5	0.05
VERITAS	33	-111	1275	4	106	499	3.5	0.1
CANGAROO	-31	137	160	3	57.3	427	4	0.3

HESS [a] is an array of 4 12-meter diameter telescopes located in the Khomas highlands of Namibia. HESS was completed at the end of 2003. The typical angular resolution of the HESS instrument of 0.1 deg . allows to make detailed images of extended galactic objects such as the supernova remnant RXJ1713-3946[6]. The HESS collaboration is performing a galatic survey of TeV sources[7] which takes advantage of both the angular resolution and the large 5 deg field of view (FOV) of the cameras. A fifth telescope with a 28-meter diameter is being built and should be completed in 2009.

The VERITAS[b] array is an upgrade of the 1O-meter Whipple telescope. The Whipple telescope was a major IACT of the 1980s and 1990s. VERITAS is very similar in caracteristics to the HESS array and was completed in 2007.

The 17 meter diameter MAGIC[c] telescope is the largest operating IACT. It is located on La Palma island in the Canaries and started its operations in 2004. It is optimised for low-energy photons ($E \simeq 50$GeV) detection. The MAGIC collaboration is building a second similar telescope which should be completed in 2008. This second telescope will allow the MAGIC collaboration to use the stereoscopy technique.

The MILAGRO[d] instrument is a shower particle detector. It is a water Cherenkov detector located at Los Alamos, at an altitude of 2630 meters. It is in operation since 2000. It has a large FOV (2 sr) which compensates for the high trigger threshold ($\sim$ 1TeV) and the angular resolution of the order of 1 deg . MILAGRO has detected extended emission from the galactic plane (Abdo et al (2008)[2]) and 4 "point sources" at a significance $> 4\sigma$ (Abdo et al (2007)[1]).

3 Galactic Centre

VHE gamma ray emission from the Galactic Centre has been reported in the TeV range by the CANGAROO, HESS, Whipple and MAGIC collaborations. The published[3] position of the TeV source HESS J1745-290 is located within 20 arc seconds of the central black hole Sgr A*. The spectrum, which was obtained from 2004-2005 data is compatible with a pure power-law with spectral index $\Gamma = 2.29 \pm 0.04(\text{stat}) \pm 0.1(\text{syst})$ in the range 100 GeV to 10 TeV. The possible non-standard interpretation of the HESS J1745-290 signal as annihilation of dark matter particles has been investigated by the HESS collaboration (F.Aharonian et al.(2006)) [3]. The observed spectrum is not well fitted by expected dark matter annihilation spectra, implying a mostly non-dark matter origin for the signal. Assuming that the observed signal is a blend of an astrophysical source and dark matter annihilations in a Navarro-Frank-White halo, the 95 % C.L. upper limits on the velocity-weighted cross-section are $< \sigma v > \simeq 10^{-24}\text{cm}^3\text{s}^{-1}$ for a neutralino mass in the range 100 GeV to 1 TeV.

The signal of HESS J1745-290 can been interpreted by a large variety of astrophysical models

[a] Web address http://www.mpi-hd.mpg.de/hfm/HESS/HESS.html
[b] Web address http://veritas.sao.arizona.edu
[c] Web address http://wwwmagic.mppu.mpg.de
[d] Web address http://www.lanl.gov/milagro

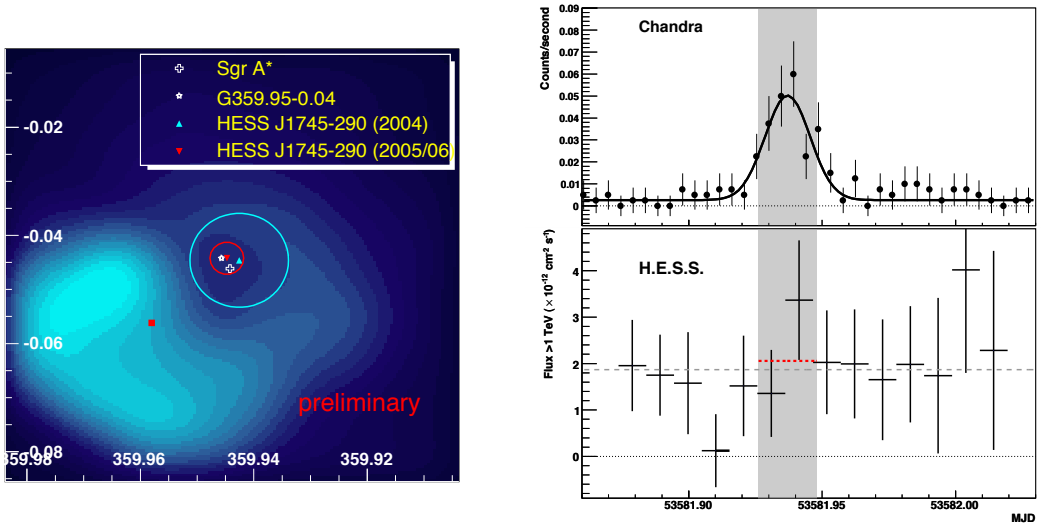

Figure 1: Left panel: VLA image of the Galactic Centre region. The extended source on the left is the supernova remnant Sgr A East. The outer circle shows the error on the position of HESS J1745-290 from F.Aharonian et al (2006). The inner circle is the error on the position of the same source from C.VanEldik et al (2007). Right panel: Simultaneous Chandra and Hess observation on July 30 2005, from J.Hinton et al (2007). Top: Chandra 1-10 keV count rate (400 seconds bins). Bottom: HESS light curve in 15 minutes bins.

(see e.g. Hinton and Aharonian (2007)[14] and references inside). Possible astrophysical sources for HESS J1745-290 include Sgr A*, the supernova remnant Sgr A East and the pulsar wind nebula G359.95-0.04. Recently, a careful study [20] allowed to lower the pointing errors of the HESS experiments down to the level of 8 arc seconds. The preliminary position of the source is located at an angular distance of $7.3\ '' \pm 8.7\ ''(\mathrm{stat}) \pm 8.5''(\mathrm{syst})$ from the central galactic black hole Sgr A*. This position (see figure 1) is incompatible with the centroid of the radio emission of the supernova remnant Sgr A East, but still compatible with sources such as the pulsar wind nebula G359.95-0.04.

The Sgr A* black hole is well known to be a variable source in the infrared and X-ray passbands. The variability of the HESS J1745-290 source has been studied in M.Vivier et al. [21]. No significant variability or periodicity was found between 30 seconds and one year. Simultaneous data were also taken with the Chandra satellite during a flare of SgrA* on July 30 2005 (see figure 1 and J.Hinton et al. (2007)[15]). No significant TeV flare was seen during the X-Ray flare. This implies that the TeV emission is produced at a relatively large distance for the Sgr A* black hole.

4 Indirect dark matter searches

Popular particle physics models such as the Minimal Supersymmetric Standard Model (MSSM) or Universal Extra Dimensions ("Kaluza-Klein" [18]) predict WIMP (Weakly Interacting Massive Particles) dark matter annihilations in galactic halos. These annihilations could give observable signals in Cherenkov telescopes (for a review see Bertone, Hooper and Silk (2005)[12]). The flux $\mathrm{d}\Phi/\mathrm{d}E_\gamma$ of gamma rays is

$$\frac{\mathrm{d}\Phi}{\mathrm{d}E_\gamma} = \frac{1}{4\pi}\frac{\mathrm{d}N_\gamma}{\mathrm{d}E_\gamma}\frac{<\sigma v>}{M_\chi^2}\bar{J}\Delta\Omega. \quad (1)$$

It is the product of an astrophysical term $\bar{J}$ and a particle physics term. The former depends on the mass density profile ρ of the dark halo

$$\bar{J} = < \int_{l.o.s} \rho^2 \mathrm{d}s > . \quad (2)$$

In equation 2, the average is taken over the solid angle $\Delta\Omega$ spanned by the Point Spread Function (PSF). The spatial resolution of H.E.S.S. is of the order of 5 arc minutes per event, giving $\Delta\Omega = 2\ 10^{-5}$. The particle physics term depends on the velocity averaged annihilation cross section $< \sigma v >$ and the WIMP mass M_χ.

The possible targets for WIMP annihilation searches can be ranked according to their values of $\bar{J}$. If the annihilation signal from a halo located at distance D is "point-like", then $\bar{J} \propto M^2/D^5$ where M is the (often measured) dark mass inside the PSF. The best astrophysical targets are thus the Galactic Center and nearby dwarf galaxies. The results of the Galactic center search have already been mentionned (section 3). Data towards several dwarf galaxies have been taken by the Atmospheric Cherenkov collaborations. These galaxies are Sagittarius (HESS[5]), Draco (MAGIC[9] and Whipple[22]) and Ursa minor (Whipple [22]). The expected flux from galaxy clusters such as Virgo or Coma is smaller by at least 3 orders of magnitude. It is also possible to look for dark matter clumps or dark matter annihilations in the vicinity of Intermediate Mass Black Holes [4].

The Sgr dwarf galaxy is a satellite of the Milky Way. It is located in the galactic plane in the direction of the Galactic Center, at a distance of 24 kpc. It is being torn apart by the tidal force of the Galaxy. The visible mass profile of the Sgr dwarf galaxy is difficult to obtain because of the contamination of galactic foreground stars. The center of the Sgr dwarf galaxy is coincident with the globular cluster M 54 [16]. The interpretation of velocity dispersion measurements is difficult because of the tidal interaction with the Milky Way. The central velocity dispersion has been measured by several groups (see e.g. Zaggia et al (2004) [23]). The HESS collaboration (F.Aharonian et al (2008) [5]) choose to describe Sagittarius galactic structure with two models. The first one is a Navarro-Frank-White model with parameters taken from Evans,Ferrer and Sarkar (2004) [13]. The other model ("core model") was fitted to the structural parameters (distribution of visible mass and central dispersion).

The Sgr dwarf galaxy has been observed by H.E.S.S. in June 2006. After quality cuts, a total exposure of 11 hours was obtained. No significant excess is seen at the position of M54. This translates into 95% C.L. upper limits of $< \sigma v > \simeq 10^{-23}\mathrm{cm}^3\mathrm{s}^{-1}$ for the NFW model and $< \sigma v > \simeq 2\ 10^{-25}\mathrm{cm}^3\mathrm{s}^{-1}$ in the "core model". These upper limits are valid in the 100 GeV - 1 TeV neutralino mass range.

The distance to the Draco dwarf galaxy is 80 kpc, more than 3 times the distance to the Sgr dwarf galaxy. On the other hand,the galactic structure of the Draco dwarf galaxy has been studied in details (see e.g Strigari et al (2007)[19], resulting in much smaller error bars on the astrophysical factor $\bar{J}$. The MAGIC and Whipple collaboration have published results on the Draco dwarf galaxy. The MAGIC collaboration has analyzed 7.8 hours of their data. They reach a sensitivity of $< \sigma v > \simeq 10^{-22}\mathrm{cm}^3\mathrm{s}^{-1}$ for neutralino masses in the range 140 GeV - 500 GeV. The Whipple collaboration reaches a sensitivity of $< \sigma v > \simeq 10^{-21}\mathrm{cm}^3\mathrm{s}^{-1}$ with 14.3 hours, for a neutralino mass in the range 500 GeV -2 TeV. They have also analyzed 17.2 hours of data towards the Ursa Minor dwarf galaxy. Their Ursa Minor upper limit is worse than their Draco limit by a factor of 2.

5 Bounds on Lorentz invariance violation

More than 15 AGN have been detected in the TeV regime. Most of them have jets directed along the line of sight (they are member of the so-called "blazar" class). The only known exception

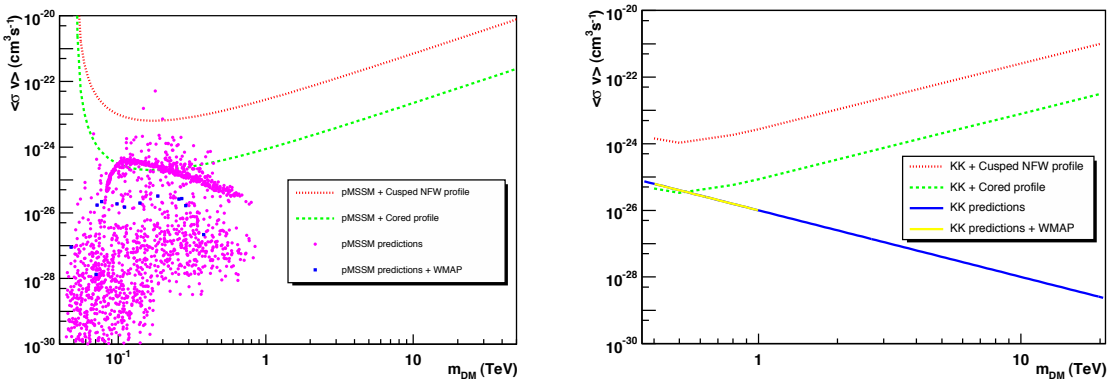

Figure 2: Results for HESS dark matter annihilations search towards the Sagittarius dwarf galaxy (Aharonian et al (2008)). Left panel: 95 % C.L. exclusion limits on MSSM models from HESS searches towards the Sgr dwarf galaxy. Right panel:95 % C.L. exclusion limits on the Universal Extra Dimensions model of Servant and Tait.

is the AGN associated to the M87 galaxy. This AGN has been observed in the TeV regime by the HEGRA, HESS, and VERITAS arrays.

The variability of the VHE emission of AGN can be used to test for Lorentz invariance in photon propagation. This is motivated by several quantum gravity theories (see Sarkar (2002)[17] for a review) in which photons and neutrinos are expected to have an energy dependent velocity in vacuum. The photon velocity $v(E)$ is parametrized by either a linear

$$v(E) = 1 - \eta \left(\frac{E}{M_1}\right) \tag{3}$$

or quadratic

$$v(E) = 1 - \eta \left(\frac{E}{M_1}\right)^2 \tag{4}$$

fonction of the energy E. $M_{1,2}$ is the scale of Lorentz invariance breaking. For quantum gravity theories, $M_{1,2}$ are expected to be of the order of the Planck scale.

An experiment observing two photons with an energy difference of ΔE, arriving from a source at distance L (or redshift $z = L/500$Mpc) in a burst of duration Δt_{burst} is sensitive to a Lorentz invariance breaking scale

$$M_1 = \frac{L\Delta E}{c\Delta t_{burst}} = 10^{18}\text{GeV}\left(\frac{z}{0.1}\right)\left(\frac{\Delta E}{1\text{TeV}}\right)\left(\frac{60\text{s}}{\Delta t_{burst}}\right) \tag{5}$$

Equation 5 shows that Lorentz invariance breaking effects can be observed in short TeV photon bursts from AGN. The MAGIC collaboration has observed flares from Mkn501 [10], an AGN at a redshift of z=0.034. A very intense flare, with a VHE photon flux of more than 3.5 times the flux of the Crab nebula occured on July 9 2005 (figure 3). The outburst lasted 15 minutes, with a flux doubling time of $\sim$ 2 minutes. The time of the flare maximum t_{max} was observed to depend on the energy. The slope of the time delay as a function of the energy is $\tau_1 = 0.030 \pm 0.012$s/GeV, in the case of a linear dependence. In other words, there is a positive 2σ positive detection, (explanable by the astrophysical emission process) which gives [11] a lower limit on $M_1 > 0.26\ 10^{18}$ GeV (95% C.L). A similar analysis gives a lower limit on $M_2 > 0.39\ 10^{11}$ GeV (95% C.L).

The HESS collaboration has observed an intense flare[8] (more than 10 times the flux of the Crab nebula) from the blazar PKS2155-304, at a redshift of z=0.116. The flare, shown on figure 3, occured on July 28 2006, was roughly 1 hour long and composed of at least 5 smaller

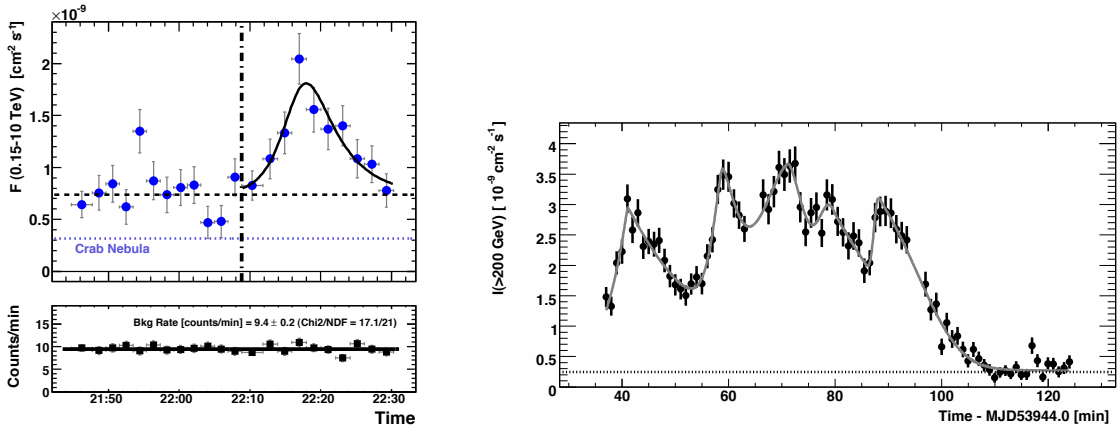

Figure 3: Left panel: MAGIC data taken during the July 9 2005 Mkn501 flare (from Albert et al (2007)). Right panel:HESS data taken during the July 28 2006 PKS2155-304 flare (from Aharonian et al (2007)).

outbursts. The shortest rise time was measured to be $\Delta t_{rise} = 173 \pm 28$ s. An analysis similar to the MAGIC analysis of Mkn501 is undergoing to improve their bounds on Lorentz invariance breaking scales.

6 Conclusion and perspectives

The VHE instruments, mostly IACT, have published a number of interesting new results. The Galactic Center source, HESS J1745-290 is probably not dark matter annihilations. It is not associated to the Sgr A East remnant. If associated to Sgr A*, the TeV emission is produced at a larger distance from the black hole than the X-ray emission. New results on indirect dark matter searches include limits from HESS towards Sgr dwarf, MAGIC and Whipple towards Draco and Whipple towards Ursa Minor. The MAGIC collaboration has given lower limits on the Lorentz invariance breaking scale based on the observation of a flare of Mkn501.

Three new instruments are coming very soon. The GLAST satellite was sucessfully launched on June 11 2008. The secong MAGIC telescope will be installed by the end of the year. Finally, the large 28-meter telescope of HESS will be completed in 2009. New astroparticle results from VHE instruments are likely to come soon.

References

1. ,A.A.Abdo *et al*, ApJ **664L**, 91 (2007)
2. , A.A.Abdo *et al*,arXiv0805.0417 (2008)
3. F.Aharonian *et al*, PRL **97**, 221102 (2006)
4. F.Aharonian *et al*, accepted for publication in PRD (2008)
5. F.Aharonian *et al*,Astroparticle Physics, **29**, 55 (2008)
6. F.Aharonian *et al*, Astronomy and Astrophysics, **449**,223(2006)
7. F.Aharonian *et al*,ApJ **636**, 777 (2006)
8. F.Aharonian *et al*,ApJ **664L**, 71 (2007)
9. J.Albert *et al*, ApJ **679**, 428 (2008)
10. J.Albert *et al*, ApJ **669**, 862 (2007)
11. J.Albert *et al*, arXiv:0708.2889 (2007)
12. G. Bertone, D. Hooper & J. Silk, Phys. Rep. **405**, 279 (2005)
13. N.W Evans, F. Ferrer and S. Sarkar, PRD **69**, 123501 (2004)

14. J. Hinton, and F. Aharonian, ApJ **657**, 302 (2007)
15. J.Hinton,M.Vivier,R.Buhler *et al*, in *proceedings of the* 30^{th} *ICRC conference, Merida (2007)*,arXiv:0711.3682
16. L. Monaco, M. Bellazzini, F. Ferraro and E.Pancino, MNRAS **356** 1396 (2005)
17. S.Sarkar, MPLA, **17**, 1025 (2002)
18. G. Servant, T.M.P Tait, Nucl.Phys.B **650**, 391 (2003)
19. L.Strigari, S. Koushiappas, J.Bullock and M. Kaplinghat, PRD **75**, 083526 (2007)
20. C.Van Eldik *et al*, in *proceedings of the* 30^{th} *ICRC conference, Merida (2007)*, arXiv:0709.3729
21. M.Vivier, O. De Jager and J. Hinton, in *proceedings of the* 30^{th} *ICRC conference, Merida (2007)*
22. M.Wood *et al*, ApJ **678**, 594 (2008)
23. S. Zaggia *et al*, Mem. Soc. Astr. it. Suppl. **5**, 291 (2004)

Solar axion search with the CAST experiment

S. Borghi[1 a b], E. Arik[17 c d], S. Aune[2], D. Autiero[1 e], K. Barth[1], A. Belov[10], B. Beltrán[5 f], G. Bourlis[g], F. S. Boydag[17 d], H. Bräuninger[4], G. Cantatore[18],J. M. Carmona[5], S. Cebrián[5], S. A. Cetin[17], J. I. Collar[6], T. Dafni[2 h], M. Davenport[1], L. Di Lella[1 i], O. B. Dogan[17 c d], C. Eleftheriadis[7], N. Elias[1], G. Fanourakis[8], E. Ferrer-Ribas[2], H. Fischer[9], J. Franz[9], J. Galán[5], E. Gazis[20], T. Geralis[8], I. Giomataris[2], S. Gninenko[10], H. Gómez[5], M. Hasinoff[11], F. H. Heinsius[9], I. Hikmet[17 d], D. H. H. Hoffmann[3], I. G. Irastorza[2,5], J. Jacoby[12], K. Jakovčić[14], D. Kang[9], T. Karageorgopoulou[20], M. Karuza[18], K. Königsmann[9], R. Kotthaus[13], M. Krčmar[14], K. Kousouris[8 j], M. Kuster[3,4], B. Lakić[14], C. Lasseur[1], A. Liolios[7], A. Ljubičić[14], V. Lozza[18], G. Lutz[13], G. Luzón[5], D. Miller[6], A. Morales[5 d], J. Morales[5], T. Niinikoski[1], A. Nordt[3,4], A. Ortiz[5], T. Papaevangelou[1 k], M. Pivovaroff[16], A. Placci[1], G. Raiteri[18], G. Raffelt[13], H. Riege[1], A. Rodríguez[5], J. Ruz[5], I. Savvidis[7], Y. Semertzidis[15], P. Serpico[13], S. K. Solanki[19], R. Soufli[16], L. Stewart[1],M. Tsagri[15], K. van Bibber[16], J. Villar[5], J. Vogel[9], L. Walckiers[1], K. Zioutas[15,1], [CAST Collaboration]

1. European Organization for Nuclear Research (CERN), Genève, Switzerland
2. IRFU, Centre d'Études Nucléaires de Saclay (CEA-Saclay), Gif-sur-Yvette, France
3. Technische Universität Darmstadt, IKP, Darmstadt, Germany
4. Max-Planck-Institut für extraterrestrische Physik, Garching, Germany
5. Instituto de Física Nuclear y Altas Energías, Universidad de Zaragoza, Zaragoza, Spain
6. Enrico Fermi Institute and KICP, University of Chicago, Chicago, IL, USA
7. Aristotle University of Thessaloniki, Thessaloniki, Greece
8. National Center for Scientific Research "Demokritos", Athens, Greece
9. Albert-Ludwigs-Universität Freiburg, Freiburg, Germany
10. Institute for Nuclear Research (INR), Russian Academy of Sciences, Moscow, Russia
11. Department of Physics and Astronomy, University of British Columbia, Vancouver, Canada
12. J. Wolfgang Goethe-Universität, Institut für Angewandte Physik, Frankfurt am Main, Germany
13. Max-Planck-Institut für Physik, München, Germany
14. Rudjer Bošković Institute, Zagreb, Croatia
15. Physics Department, University of Patras, Patras, Greece
16. Lawrence Livermore National Laboratory, Livermore, CA, USA
17. Dogus University, Istanbul, Turkey
18. Sezione INFN di Trieste and Università di Trieste, Trieste, Italy
19. Max-Planck-Institut für Aeronomie, Katlenburg-Lindau, Germany
20. National Technical University of Athens, Athens, Greece

[a] Attending speaker. Email: Silvia.Borghi@cern.ch
[b] Present address: University of Glasgow, Glasgow, UK
[c] Present address: Bogazici University, Istanbul, Turkey
[d] deceased
[e] Present address: Institute de Physique Nucléaire, Lyon, France
[f] Present address: Department of Physics, Queen's University, Kingston, Ontario
[g] Present address: Hellenic Open University, Patras,Greece
[h] Present address: Instituto de Física Nuclear y Altas Energías, Universidad de Zaragoza, Zaragoza, Spain
[i] Present address: Scuola Normale Superiore, Pisa, Italy
[j] Present address: Fermi National Accelerator Laboratory, Batavia, Illinois 60510
[k] Present address: IRFU, Centre d'Études Nucléaires de Saclay (CEA-Saclay), Gif-sur-Yvette, France

The CAST (CERN Axion Solar Telescope) experiment is searching for solar axions by their conversion into photons inside the magnet pipe of a LHC prototype dipole. In the phase II, CAST is operating with a buffer gas inside the magnet bore apertures in order to extent the sensitivity of the experiment to larger axion masses. Preliminary results from the analysis of this second phase with ^{4}He inside the magnet pipes excludes axions down to $g_{a\gamma} < 2.2 \cdot 10^{-10}$GeV^{-1} at 95% C.L. for $0.02\ e\text{V} < m_a < 0.39\ e\text{V}$. The data analysis has resulted in the most restrictive experimental limit on the coupling constant of axions to photons and for the first time experimental result has entered the theory motivated axion parameter space. At the beginning of 2008, data started to be taken with ^{3}He in the magnet pipes in order to extend the sensitivity to axion masses up to 1.2 eV.

1 Introduction to Axion Theory

In the Standard Model, the QCD Lagrangian [1] includes a gluon interaction term that violates charge conjugation times parity (CP) and time reversal (T):

$$\mathcal{L}_{CP} = \bar{\theta}\frac{\alpha_s}{8\pi}G\widetilde{G} \tag{1}$$

where G is the color field strength tensor, $\widetilde{G}$ its dual, $\bar{\theta}$ represents the effective QCD vacuum and it can assume any value between 0 and 2π. A non vanishing $\bar{\theta}$ value would imply CP violation.

Evidence of CP violation would be observable by the electric dipole moment of neutrons, that has been theoretically estimated to be [2]:

$$d_n \approx \bar{\theta}\frac{e}{m_n}\frac{m^*}{\Lambda_{QCD}} \propto \bar{\theta} \cdot 3.6 \cdot 10^{-16} e\,\text{cm} \tag{2}$$

where Λ_{QCD} is QCD energy scale ≈ 1 GeV and m^* is the reduced mass of the up and down quark defined as $m^* = \frac{m_u m_d}{(m_u+m_d)}$, m_n is the neutron mass, e the unit electrical charge. The present experimental upper limit [3] however, is smaller than

$$d_n < 2.9 \cdot 10^{-26} e\,\text{cm}\ (90\%\ CL) \tag{3}$$

Consequently, the phase parameter $\bar{\theta}$ should be smaller than 10^{-10}. This implies that CP is not very strongly broken in the strong interactions. So the solution of the $U(1)_A$ problem begets a different problem: why is CP not badly broken in QCD? This is known as the strong CP problem.

One solution was proposed by Peccei Quinn in 1977 [4] introducing a new global chiral U(1)$_{PQ}$ symmetry. This symmetry is necessarily spontaneously broken at an unknown scale f_a, and its introduction into the theory effectively replaces the static CP-violating angle $\bar{\theta}$ with a dynamical CP- conserving field - the axion. Formally, to make the Lagrangian of the Standard Model U(1)$_{PQ}$ invariant this Lagrangian must be increased by axion interaction:

$$\mathcal{L}_a = -\frac{1}{2}\left(\partial a\right)^2 + \frac{\alpha_s}{8\pi f_a}\, a\, G\widetilde{G} \tag{4}$$

where α_s is the strong coupling constant, a is the axion field, f_a the axion decay constant and $f_a \propto \frac{1}{g_{a\gamma\gamma}}$. Color anomaly factors have been absorbed in the normalization of f_a which is defined by this Lagrangian. Non-perturbative effects induce a potential for a whose minimum is at $a = \bar{\theta} f_a$, thereby canceling the $\bar{\theta}$ term in the QCD Lagrangian, and thus allowing for the dynamical restoration of the CP symmetry.

Weinberg [5] and Wilczek [6] realized that a consequence of this mechanism is a new pseudo-scalar boson, the axion, which is the Nambu-Goldstone boson of the PQ symmetry. The axion coupling to ordinary matter is proportional to the axion mass m_a and, equivalently, to the inverse of the PQ scale $1/f_a$. The PQ symmetry is explicitly broken at low energies by instantaneous effects so that the axion acquires a small mass:

$$m_a = \frac{z^{1/2}}{1+z} \frac{f_\pi m_\pi}{f_a} \approx 6\ e\mathrm{V} \frac{10^6 \mathrm{GeV}}{f_a} \tag{5}$$

where f_π is the pion decay constant and $z = m_u/m_d$ is the mass ratio of up and down quarks (for this numerical estimate [7] we used a canonical value of z=0.56). Depending of their density and mass, axions may constitute a candidate for the cold dark matter in the universe.

One generic property of the axion is a two-photons interaction that plays a key role for most searches:

$$\mathcal{L}_{a\gamma} = \frac{1}{4} g_{a\gamma} F \widetilde{F}\ a = -g_{a\gamma} \mathbf{E} \cdot \mathbf{B}\ a \tag{6}$$

where F is the electromagnetic field-strength tensor, $\widetilde{F}$ its dual, $\mathbf{E}$ and $\mathbf{B}$ the electric and magnetic fields. The coupling constant is:

$$g_{a\gamma} = \frac{\alpha}{2\pi f_a} \left(\frac{E}{N} - \frac{2}{3} \frac{4+z}{1+z} \right) \tag{7}$$

where α is the fine structure constant, E and N are the electromagnetic and color anomaly of the axial current associated with the axion field and E/N is a model dependent parameter [8].

2 Solar Axions

Axions could be produced in stellar cores through their coupling to plasma photons, namely by Primakoff conversion [9], with energies in the range of keV. The expected solar axion flux on earth based on a Standard Solar Model (see fig.1) is well approximated by [10]:

$$\frac{d\Phi}{dE} = \left(\frac{g_{a\gamma\gamma}}{10^{-10} \mathrm{GeV}^{-1}} \right)^2 \Phi_0 \frac{E^{2.481}}{e^{E/(1.205)}} \tag{8}$$

where E is in keV and $\Phi_0 = 6.020 \cdot 10^{10}\ \mathrm{cm}^{-2}\mathrm{s}^{-1}\mathrm{keV}^{-1}$. The maximum of the distribution is at 3.0 keV and the average energy is 4.2 keV.

This flux can be searched with the inverse process described by (6) where an axion converts into a photon in a macroscopic magnetic field [12]. The conversion probability in magnetic field region in vacuum is given by [13]

$$P_{a\to\gamma} \approx (BLg_{a\gamma\gamma})^2 \frac{\sin^2(qL/2)}{(qL)^2} \tag{9}$$

where B is the magnetic field strength, L is the path length, q is the momentum transfer between the axion and the X-ray photon $q = \frac{m_a^2}{2E_a}$, E_a is the axion energy. The conversion is coherent over a large propagation distance for $qL \ll 1$.

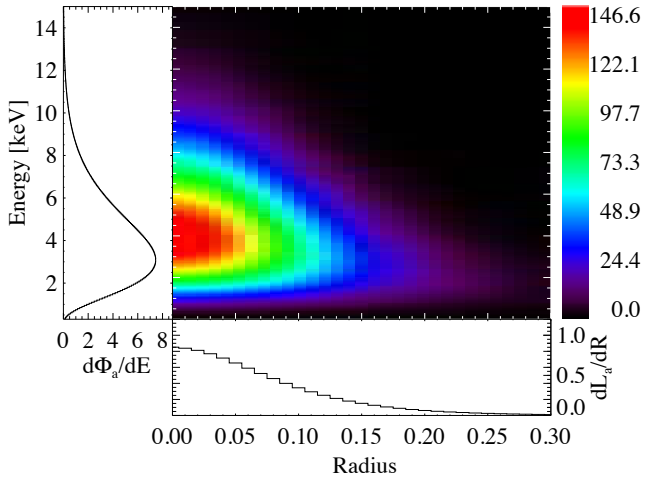

Figure 1: Axion surface luminosity seen from the Earth as a function of axion energy and the radius where the axion are produced in the sun normalized to the solar radius. [11]

One could reach sensitivity for larger axion masses by filling the magnetic field region with a gas, consequently the photon acquires an effective mass, and the conversion probability is [14]

$$P_{a\to\gamma} \propto \left(\frac{BLg_{a\gamma\gamma}}{2}\right)^2 \frac{1}{q^2+\Gamma^2/4}\left[1+e^{-\Gamma L}-2e^{-\Gamma L/2}\cos(qL)\right] \tag{10}$$

where Γ is the inverse photon absorption length for the X-rays in the medium, q is the momentum transfer $q = \frac{m_\gamma^2 - m_a^2}{2E_a}$, E_a is the axion energy, m_γ is the photon effective mass in the buffer gas that depends on the type and density of gas:

$$m_\gamma \approx \sqrt{\frac{4\pi\alpha N_e}{m_e}} = \sqrt{\frac{Z}{A}\rho} \tag{11}$$

where Z and A are the atomic and mass number of the gas, m_e is the electron mass, N_e is the number of electron per cm^3 and ρ is the gas density. The coherence $qL < \pi$ can be restored for a narrow mass range:

$$\sqrt{m_\gamma^2 - \frac{2\pi E_a}{L}} < m_a < \sqrt{m_\gamma^2 - \frac{2\pi E_a}{L}}. \tag{12}$$

The choice of a specific gas pressure allows the test of a specific axion mass. Scanning over a range of pressure means scanning over a large range of axion mass.

3 CAST

The CAST [15,16] (CERN Axion Solar Telescope) experiment uses a decommissioned LHC prototype supercoducting magnet with a length of 9.26 m, a magnetic field of about 9 T inside two beam pipes. The magnet is mounted on a moving platform allowing a vertical movement of $\pm 8°$ and an horizontal movement of $\pm 40°$. Different detectors are mounted at the two ends of the magnet cryostat The magnet can point to the sun core for about 1.5 hour at the sunrise and at the sunset, when the magnet is not aligned with the sun the time is dedicated to background measurements. The detectors cover about $1/10^{\text{th}}$ of the solar radius, searching for the axion potentially emitted by the solar core. The CAST tracking system has been accurately calibrated by geometric survey measurements and it is verified by a sun filming. The pointing precision is evaluated to be better than $0.01°$.

On one end of the magnet, a conventional plexigas Time Projection Chamber (TPC) [17 18], covering both beam pipes, looks for X-rays coming from axion-to-photon conversion during the sunset. On the opposite magnet end, a Micro-Mesh Gaseous detector (MM) [19] and a Charge Coupled Device (CCD) [20] look for X-rays during the sunrise. The CCD is located at the end of X-ray telescope designed for the German X-ray satellite mission ABRIXAS [21]. This telescope focuses the photons from the magnet bore with a 14.5 cm^2 aperture to a spot size of about 6 mm^2 on the CCD, and thus improving the signal to background ratio by a factor of about 150.

4 Result

During the phase I (2003-2004 data taking) the CAST experiment was operated keeping the magnet pipes evacuated and therefore it was sensitive to the axion mass range up to $m_a = 0.02eV$ due to coherence effects. The results of phase I improved the limit of the axion coupling constant by a factor of 7 with respect to the previous experimental searches and it went beyond the astrophysical limit of globular clusters for coherence masses [11].

The phase II of CAST, where the magnet pipes are filled with a buffer gas, can extend the sensitivity to higher axion rest masses. During 2005, the experiment was upgraded to allow the injection of a buffer gas in the cold bores. A new gas system was built and has been operation since the end of 2005. This system gets a density stability, an accuracy of pressure of about 0.2 mbar and a reproducibility precision of 0.01 mbar. The data taking of phase II with ^{4}He during 2005 and 2006 covered one different pressure per day for a total of 160 density steps (step size is about 0.083 mbar at 1.8 K) up to 13 mbar, near the condensation limit of ^{4}He gas at the

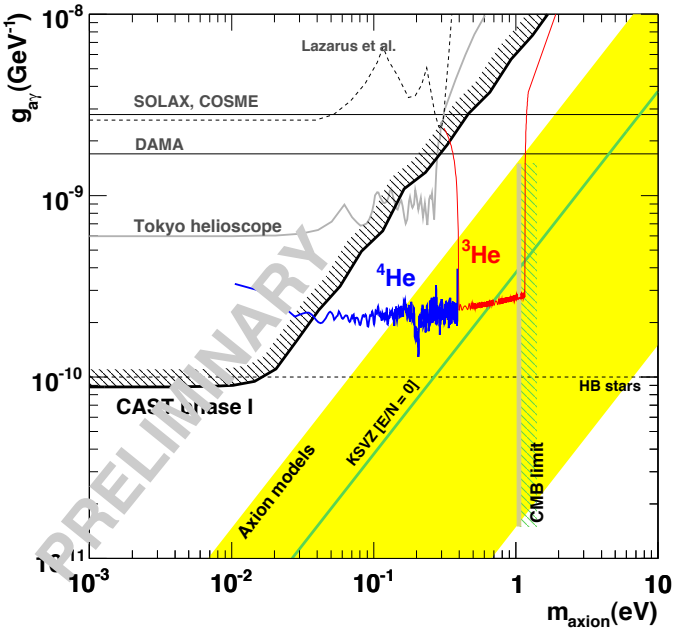

Figure 2: 95% C.L. exclusion line in the axion/photon coupling constant versus the axion mass plane obtained from the complete CAST phase I data [11] (line labeled "CAST Phase I"), from phase II with ^{4}He (blue line labeled "^{4}He") and the foreseen sensitivity for CAST phase II with ^{3}He (red line labeled "^{3}He"). These results are compared with other laboratory limits such as previous helioscopes Lazarus et al. [22], the Tokyo [23] helioscope and those obtained from axion experiments with crystalline detectors located underground (SOLAX [24], COSME [25] and DAMA [26]) and other constraints like the horizontal branch (HB) stars [27]. The grey band labeled "CMB limit" represents the limit evaluated by the amount of Hot Dark Matter deduced by the cosmic microwave background data [28]. The yellow band represents typical theoretical models with $|E/N - 1.95|$ in the range $0.07 - 7$ while the green solid line corresponds to the case when $E/N = 0$ is assumed.

operation temperature of 1.8 K that is about 16 mbar. This corresponds to a scan of axion mass range between 0.02 eV up to 0.39 eV. The preliminary combined results of ^{4}He data for all three detectors are shown in fig.2. The average upper limit to the axion-photon coupling at 95% C.L., in the axion mass range 0.02 eV up to 0.39 eV, is $g_{a\gamma} < 2.2 \cdot 10^{-10}Ge$V^{-1}. For the first time experimental results entered in the QCD theoretically allowed axion models region.

During 2007 the experiment was upgraded to allow the injection of ^{3}He as buffer gas. This gas can reach pressures up to about 135 mbar at 1.8 K, corresponding to axion masses up to about 1.2 eV. The new automatic gas system has the same accuracy and reproducibility of the previous one and moreover it has a high safety and reliability level required to have no leaks of this gas, considerable expensive. The new gas system is operational since end of 2007. In parallel with the above mentioned upgrade, CAST improved the detector system replacing the TPC and MM by MicroMegas detectors based on the new bulk and microbulk technology. These detectors have a better energy resolution and a better background rejection. The new detectors are covered by a shielding composed of copper, lead, cadmium, nitrogen and polyethylene allowing background reduction by a factor 3. The data taking for phase II with ^{3}He started in March 2008. CAST plans to run during the next 3 years to fully exploit the region up to axion mass of 1.2 eV, entering deeper into the QCD theoretically axion models space up to the region excluded by the amount of Hot Dark Matter induced by the cosmic microwave background data [28] (CMB). The expected reachable region is shown in fig. 2.

5 Conclusion

The CAST experiment has been running in phase I (vacuum in the beam pipe in 2003 and 2004) yielding to a lower limit on $g_{a\gamma} < 8.8 \cdot 10^{-11}Ge$V^{-1} at 95% C.L. for axion masses $m_a < 0.02\,e$V. During 2005, a major modification to the magnet pipe system was undertaken to fill the beam pipes with ^{4}He during 2005 and 2006. A new system was commissioned and installed in 2007 to use as buffer gas ^{3}He allowing to exploit the region up to axion mass of 1.2 eV. The preliminary results of phase II with ^{4}He has been presented, the average upper limit to the axion-photon coupling is $g_{a\gamma} < 2.2 \cdot 10^{-10}Ge$V^{-1} at 95% C.L. for axion masses $0.02\,e\text{V} < m_a < 0.39\,e$V. These results improve the previous constraints given by other experiments by a factor of 7 and have entered the theory motivated axion parameter space. The ^{3}He phase, with data taking started in March 2008, allows to enter deeper in the theoretical axion model allowed phase space and will continue for about three years.

References

1. C. Quigg, *Gauge Theories of the Strong, Weak and Electromagnetic Interactions* (Addison Wesley, 1982).
2. M. Pospelov and A. Ritz, *Astron. Astrophys.* **318**, 119 (2005).
3. C.A. Baker *et al.*, *Phys. Rev. Lett.* **97**, 131801 (2006).
4. R. D. Peccei and H. R. Quinn, *Phys. Rev. Lett.* **38**, 1440 (1977), *Phys. Rev. Lett.* **16**, 1791 (1977).
5. S. Weinberg, *Phys. Rev. Lett.* **40**, 223 (1978).
6. F. Wilczek, *Phys. Rev. Lett.* **40**, 279 (1978).
7. J. Gasser and H. Leutwyler, *Phys. Rept.* **87**, 77 (1982).
8. S. L. Cheng, C. Q. Geng and W. T. Ni, *Phys. Rev.* D5231321995.
9. H. Primakoff, *Phys. Rev.* **81**, 899 (1951).
10. G. G. Raffelt *hep-ph/0611350* (2007).
11. S. Andriamonje *et al.*, *J. of Cosmol. and Astropart. Phys.* **04**, 010 (2007).
12. P. Sikivie , *Phys. Rev. Lett.* **51**, 1415 (1983).

13. K. Van Bibber *et al.*, *Phys. Rev. Lett.* **59**, 759 (1987).
14. K. Van Bibber *et al.*, *Phys. Rev.* D **39**, 2089 (1989).
15. K. Zioutas *et al.* , *Nucl. Instrum. Methods* A **425**, 480 (1999).
16. K. Zioutas *et al.* , *Phys. Rev. Lett.* **94**, 121301 (2005).
17. D. Autiero *et al.* , *New J. Phys.* **9**, 171 (2007).
18. D. Autiero *et al.* , *New J. Phys.* **9**, 208 (2007).
19. P. Abbon *et al.* , *New J. Phys.* **9**, 170 (2007).
20. M. Kuster *et al.* , *New J. Phys.* **9**, 169 (2007).
21. J. Altmann et al., *Proc. SPIE* **3444**, 350 (1998); Egle et al., *Proc. SPIE* **3444**, 359 (1998); W. J. Egle, J. Altmann and H. Schwarz, *Proc. SPIE* **3766**, 2 (1999).
22. D. Layarus *et al.*, *Phys. Rev.* D **39**, 2089 (1989).
23. S. Morizama *et al.*, *Phys. Lett.* B **434**, 147 (1998).
24. F. T. Avignone *et al.* [SOLAX Collaboration], *Phys. Rev. Lett.* **81**, 5068 (1998).
25. A. Morales *et al.* [COSME Collaboration], *Astron. Astrophys.* **16**, 325 (2002).
26. R. Bernabei *et al.*, *Phys. Lett.* B **515**, 6 (2001).
27. A. Buzzoni *et al.*, Å **128**, 94 (1983).
28. S. Hannestad, A. Mirizzi and G. Raffelt, *J. of Cosmol. and Astropart. Phys.* **0507**, 002 (2005). A. Melchiorri, O. Mena and A. Slosar, *Phys. Rev.* D **76**, 014303 (2007).

THE LOW ENERGY FRONTIER: probes with photons

J. REDONDO
DESY Theory Group, Notkestrasse 85 Bldg. 2a,
D-22603 Hamburg, Germany

I discuss different aspects of the phenomenology of hypothetical sub eV mass particles arising in the context of extensions of the standard model. I focus on a simple extension based on an additional U(1) gauge symmetry and its corresponding gauge boson, called "hidden photon". Kinetic mixing with the standard photon leads to photon-hidden photon oscillations that are searched for in laboratory experiments like ALPS at DESY. Hidden photons produced in the interior of the Sun could be also detected in axion helioscopes like CAST at CERN and could play an interesting role in late cosmology, where the presence of additional feebly interacting relativistic particles seems to be favored. All these effects disappear as the hidden photon mass decreases, allowing phenomenologically large kinetic mixings. However, in this case such a hidden photon will even play a role in gauge coupling unification.

In the days of exploring the TeV frontier, are we leaving something behind us?
It is a common opinion, and we will find numerous examples of it in this volume, that the standard model (SM) of particle physics is not completely satisfactory to describe certain aspects of nature. Extensions of the SM invoked to cure their diseases include generally many additional symmetries and fields. The corresponding particles have generally masses arranged to lay beyond the reach of our collider experiments (or just around the corner), namely beyond a TeV. It is clear that if these additional particles are very massive we have little chances of discover them in colliders, and we should rely on low energy precision experiments. *But they could be additional light particles.* On general grounds, low masses are related to some symmetry that prevents high radiative contributions from larger mass scales. It is clear that the knowledge of these hypothetical low energy particles will provide us with an understanding of their related symmetries, and guide us through the difficult task of extending the standard model to describe particle physics up to arbitrarily high energies.

Of course, when these particles couple directly to the SM its existence is severely constrained

from laboratory searches and our current understanding of astrophysics and cosmology. However, *there are certain models in which the powerful astrophysical constraints are evaded* [1].

1 Massive Hidden photons and the "meV valley"

In this contribution I focus on one of these models, whose only addition to the SM lagrangian consists in a new U(1) gauge symmetry and its corresponding gauge boson, here called "hidden photon". The SM fields are assumed to be uncharged under this new gauge group, but nevertheless they can still interact with the hidden photon through *kinetic mixing* with the standard model photon. Therefore we will consider the low energy effective lagrangian

$$\mathcal{L} = -\frac{1}{4}F_{\mu\nu}F^{\mu\nu} - \frac{1}{4}B_{\mu\nu}B^{\mu\nu} + \frac{\sin\chi}{2}B_{\mu\nu}F^{\mu\nu} + \frac{\cos^2\chi}{2}m_{\gamma'}^2 B_\mu B^\mu, \tag{1}$$

where $F_{\mu\nu}$ and $B_{\mu\nu}$ are the photon (A^ν) and hidden photon (B^ν) field strengths. The dimensionless mixing parameter $\sin\chi$ can be generated at an arbitrarily high energy scale and does not suffer from any kind of mass suppression from the messenger particles communicating between the visible and the hidden sector. This makes it an extremely powerful probe of high scale physics. The construction outlined here arises quite naturally in extensions of the SM based on string theory, where values in the range $10^{-16} \lesssim \chi \lesssim 10^{-2}$ can be expected [2].

The most prominent implication of the kinetic mixing term is that photons are no longer massless propagation modes. The kinetic mixing term can be removed by changing the basis $\{A, B\} \rightarrow \{A_{_R}, S\}$, where $A_{_R} = \cos\chi A$ is a renormalized photon field and $S = B - \sin\chi A$ is the state *orthogonal* to it, and therefore completely *sterile* with respect to electromagnetic interactions. The renormalization is typically unobservable and will be discussed in section 2. In this section we use $A = A_{_R}$. In the $\{A, S\}$ basis the kinetic term is diagonal but kinetic mixing has provided an off-diagonal mass term which produces $A-S$ (vacuum) oscillations with a probability

$$P_{A-S} = \sin^2 2\chi \sin^2 \frac{m_{\gamma'}^2 L}{4\omega} \quad . \tag{2}$$

where ω is the energy and L is the oscillation length. It also modifies the static Coulomb potential with a Yukawa-like contribution

$$V(r) = -\frac{\alpha}{r}\left(\cos^2\chi + e^{-m_{\gamma'}r}\sin^2\chi\right) \ . \tag{3}$$

The phenomenology of such a model has been considered by Okun [3] and others [4]. The stronger laboratory constraint comes from precision measurements of the Coulomb law [5] and can be read off in Fig. 1. The sensitivity of this test has a clear maximum at distances of the order of the centimeter, corresponding to $m_{\gamma'} \sim \mu$eV. For much smaller $m_{\gamma'}$ the hidden photon contribution is indistinguishable from that of a single massless photon, and for much higher $m_{\gamma'}$ the hidden photon contribution is exponentially suppressed.

Let us now consider the astrophysical bounds, focusing on the case of the Sun. Photons of the interior of the Sun can oscillate into the sterile component that can freely escape from the solar interior removing energy that otherwise will take much longer to drain. The response of the solar structure to such an exotic energy loss is to raise the temperature of the interior so that the thermonuclear reactions can provide this extra energy. The consequence is that Hydrogen is converted much faster into Helium and the duration of the Hydrogen burning period is reduced. Studies of Raffelt and Dearborn [6] concluded that such an exotic luminosity cannot be higher than the actual visible luminosity of the Sun. Therefore, integrating eq. 2 over the thermal distribution of photons over the solar interior will provide us with a limit [4,7] on χ. To proceed we only have to take into account an important subtlety: namely that photons in a plasma

propagate as massive particles with a mass given by the plasma frequency $\omega_{\rm P} = 4\pi\alpha n_e/m_e$ with α the fine structure constant and m_e, n_e the electron mass and number density. In such a case, the essential modification of the transition probability is the introduction of an effective mixing angle given, in the small χ approximation [7], by

$$\chi^2 \to \chi^2_{\rm eff} = \frac{\chi^2 m^4_{\gamma'}}{(\omega^2_{\rm P} - m^2_{\gamma'})^2 + (\omega\Gamma)^2} \tag{4}$$

which strongly suppresses $A - S$ transitions, and therefore energy drain, when $m_{\gamma'} \ll \omega_{\rm P}$. Here Γ is the photon absorption rate and cuts-off the effective mixing in the resonant regime where $m_{\gamma'} \simeq \omega_{\rm P}$ and the amplitude of the oscillations is maximum. The plasma frequency in the solar interior varies in the range 1 eV $\lesssim \omega_{\rm P} \lesssim$ 300 eV (and typically $\omega\Gamma$ is smaller), so hidden photons with masses below the eV can evade the solar luminosity bound even with relatively high values of the vacuum mixing parameter χ (See Fig. 1).

Even a low, harmless, hidden photon flux can be detectable at earth by a suitable detector. The CAST collaboration at CERN [8] (See the review of Silvia Borgi in this same Proceedings) operates a search for solar axions of keV energies by tracking the Sun with a 10 m long LHC magnet, since axions emitted from the Sun can convert into photons by the inverse Primakoff effect [9]. Such an experiment will be also sensitive to hidden photons, with the benefit that high vacuum conditions are kept in the conversion region and thus the effective mixing angle is not suppressed. This nearly background free experiment can measure a photon spectral flux generated inside the magnet of 10^{-5} photons per second, cm^2 and keV. This number was used [7] to set the hidden photon limit labeled CAST in Fig. 1. A recent paper [10] has pointed out that considerable improvement can be achieved by measuring hidden photons of lower energies $\sim$ eV where the flux is maximal since it mostly comes from the external shells of the Sun where the electron density (and hence the plasma frequency) is smallest.

The Coulomb and CAST limits leave a valley in the allowed parameter space around the suggestive mass scale of $m_{\gamma'} \simeq$ meV. Since photon-hidden photon oscillations are resonant when a plasma is present such that $\omega_{\rm P} = m_{\gamma'}$, it would be advantageous to find environments with a huge number of photons and electron densities $\sim 10^{15}$ cm^{-3}. These conditions are found in the early universe when the temperature is of order $\sim$ keV, i.e. *after big bang nucleosynthesis* (BBN) but *before the cosmic microwave background* (CMB) formation. In such a scenario a fraction of the photon background will be resonantly converted into hidden photons, forming a hidden cosmic microwave background (hCMB) [11]. This hCMB decouples much before than the standard CMB and from that moment on *mimics the effect of additional neutrino species*, $N^{\rm eff}_\nu$. Since some of the CMB photons disappear, the baryon to photon ratio η measured at decoupling also increases with respect to the value suggested by BBN. Therefore we can bound $\sim$ meV hidden photons from the agreement of the values of $N^{\rm eff}_\nu$ and η provided from BBN and CMB physics [11]. The CMB observations, combined with large scale structure data (LSS), slightly prefer [12] $N^{\rm eff}_\nu > 3$ but both frameworks can be made to coincide within the quoted errors. The preference of a high $N^{\rm eff}_\nu > 3$ is supported by the SDSS and Ly-α data and might be likely due to systematics [13]. However, even in [13] where a more careful treatment of the bias parameters is included, values slightly higher than 3 are still preferred, with a best global fit of $N^{\rm eff}_\nu = 3.8^{+2.0}_{-1.6}$ (95% C.L.). It is however premature to consider that such an excess has a physical interpretation in terms of new physics, but if eventually it is confirmed it may require new weakly interacting particles that are relativistic at CMB, namely sub eV particles, and hidden photons could certainly do the job.

Note that the conservative "suggested" excess $\Delta N^{\rm eff}_\nu \simeq 0.8$ corresponds to a hidden photon with $\chi \simeq 2 \times 10^{-6}$. The mass should be then $\simeq 0.2$ meV to avoid distortions of the CMB Plack spectrum and the laboratory searches to be presented next. At the view of Fig. 1 this leads us to a clear goal in the parameter space!

Interestingly, such a scenario is going to be tested in the near future in the laboratory. The ALPS (Any Light Particle Search) experiment at DESY [14] is currently setting up an upgraded "light-shinning-through-walls" experiment [15] that will explore much of the relevant parameter space in the "meV valley". The set up consists in a powerful laser beam which propagates under high vacuum conditions to end up blocked in an opaque wall. If hidden photons or any other weakly interacting low mass particles are produced before the wall they will go through it and can be reconverted after the wall in another high vacuum cavity in which a sensitive detector is placed. Some similar experiments have been already performed [16,17,18], the most recent motivated by the recent PVLAS episode [19] and a recent paper has interpreted them in terms of hidden photons [20]. The current ALPS proposal includes 300 W of laser power, conversion and reconversion lengths of ~ 6 meters and a small background ~ 50 mHz. The results will be presented in late fall of this same year, and immediately after several upgrades will be performed, including possibly higher laser power, a new detector and "phase shift plates" [21] to enhance the coherence between photons and hidden photons.

Already with the first upgrade the ALPS experiment will be sensitive to part of the region of major cosmological interest, and will eventually cover it completely with subsequent improvements. On the long term, additional coverage could be also provided by the mentioned new solar hidden photon searches [10] or by a photon regeneration experiment using radio waves instead of laser light [22].

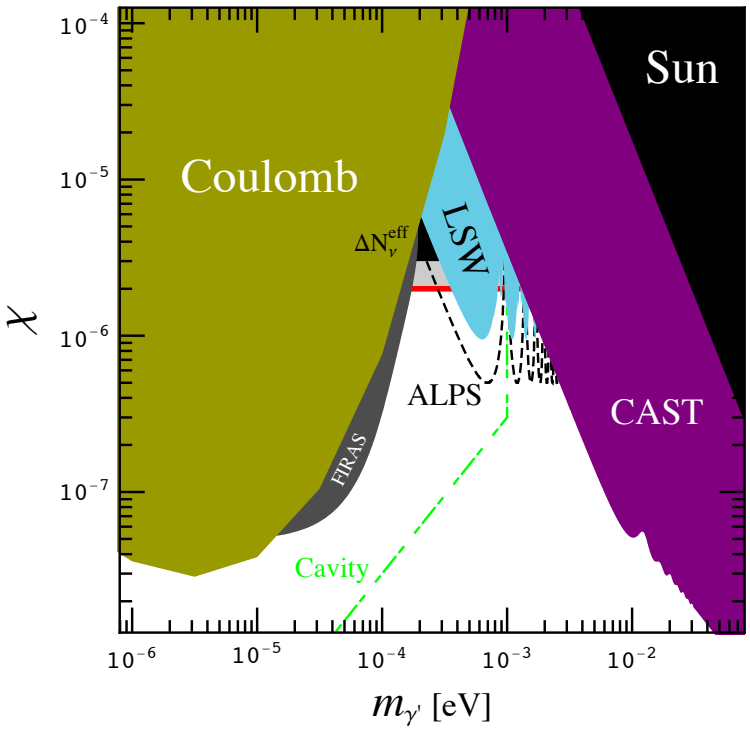

Figure 1: The "meV Valley" in the mass-mixing plane of a hidden photon is bounded at low masses by searches from deviations of the Coulomb law and from seaches of solar hidden photons with the CAST helioscope at higher masses. Light-shinning-through-walls (LSW) experiments have explored the peaceful realm around $m_{\gamma'} \sim$ meV and an upgraded ALPS setup will penetrate even deeper in the near future. In the early universe a part of the CMB can resonantly oscillate into hidden photons contributing, as neutrinos do, to the radiation density at decoupling. Values higher than $N_\nu^{\rm eff} > 5$ can be excluded, but a value slightly higher than 3, $N_\nu^{\rm eff} \simeq 3.8$ is still preferred (Red line). The precise determination of the CMB spectrum by FIRAS constraints the distortions that the creation of this hidden CMB would imprint on it. An experiment exploiting microwave cavities could be sensitive to most of the region of cosmological interest. See the text for references.

2 Massless hidden photons and Unification

All effects mentioned before are lost in the probably most natural case, a *massless* hidden photon. Well, not all of them. We have already mentioned that to get rid of the kinetic mixing and define fields with canonical kinetic terms we need to renormalize the photon field with a factor $\cos\chi$. In the low energy lagrangian considered this is harmless, since a photon renormalization is simply reabsorbed in the definition of the electric charge as usual. Even when one considers the whole standard model gauge group and allows our new U(1) gauge boson to mix with the boson of *hypercharge* (kinetic mixing with non-abelian gauge fields will not respect gauge invariance) the corresponding gauge coupling g_1 will absorb again this factor and leave no trace in precision electroweak observables.

Since this shift will only affect g_1 but not g_2 or g_3, it could be detectable in a theory in which there is an *a priori* relation between the couplings, such as in *grand unification*. In this case we shall define the unification scale by the equality of the two couplings that are unchanged $g_2(m_{\rm GUT}) = g_3(m_{\rm GUT})$. Note that we measure the "renormalized" g_1 and this is *allways larger* than the real value (the one we would expect to unify) in a factor $1/\cos\chi$, namely

$$g_1^{\rm measured} = \frac{g_1^{\rm real}}{\cos\chi} \ . \tag{5}$$

Interestingly, the measured value of g_1 in the standard model turns out to be also *larger* than the required to unify with g_2 and g_3 in a pure SU(5) model *without supersymmetry*. Therefore unification could be achieved at a scale $\simeq 10^{17}$ GeV (evading limits from proton decay) but being "masked" by the exotic hypercharge renormalization due to kinetic mixing with $\chi \simeq 0.4$. We have taken values of $g_{1,2,3}$ at the Z-pole from [23] and plotted the running in Fig. 2.

The case with supersymmetry (SUSY) is more complicated. Using the renormalization group equations at the one-loop level, a small value of $\chi \simeq 0.055$ improves the already impressive unification, but this effect is of similar magnitude than the threshold corrections of SUSY particles of ∼TeV masses and particles at the scale of unification. When these corrections are included the measured value of g_1 seems to be a bit *smaller* than the required to unify perfectly [24] (see [25] for a recent discussion). While a more detailed study is under way [26], the two possible outcomes are clear: if $g_1(m_{\rm GUT}) < g_{2,3}(m_{\rm GUT})$ a bound on χ of order 10^{-2} can be set, in the opposite case, a small value of χ could be the responsible of the difference and unification could be achieved.

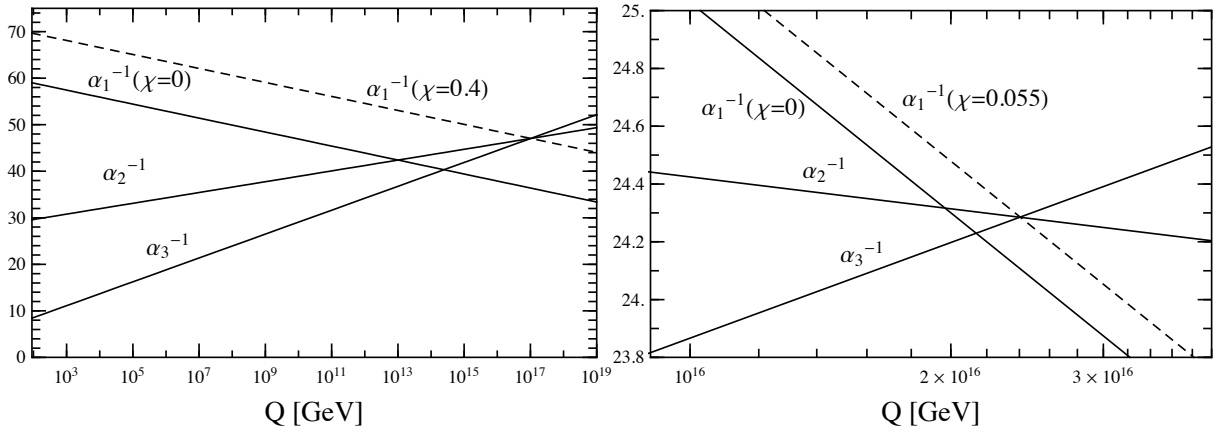

Figure 2: One-loop running of the SM gauge couplings with an exotic renormalization of the hypercharge coupling g_1 due to kinetic mixing with an additional massless U(1) gauge boson. LEFT: standard model, RIGHT: with supersymmetry. Note that $\alpha_{1,2,3} = g_{1,2,3}^2/(4\pi)$ and g_1 has been normalized with the usual SU(5) factor $\sqrt{5/3}$.

References

1. E. Masso and J. Redondo. *Phys. Rev. Lett.* **97** (2006) 151802, hep-ph/0606163; *JCAP* **0509** (2005) 015, hep-ph/0504202; J. Jaeckel, E. Masso, J. Redondo, A. Ringwald, and F. Takahashi. *Phys. Rev.* **D75** (2007) 013004, hep-ph/0610203; R. N. Mohapatra and S. Nasri. *Phys. Rev. Lett.* **98** (2007) 050402, arXiv:hep-ph/0610068; P. Brax, C. van de Bruck, and A.-C. Davis. *Phys. Rev. Lett.* **99** (2007) 121103, hep-ph/0703243.
2. K. R. Dienes, C. F. Kolda, and J. March-Russell. *Nucl. Phys.* **B492** (1997) 104–118, hep-ph/9610479; S. A. Abel, J. Jaeckel, V. V. Khoze, and A. Ringwald. arXiv:hep-ph/0608248; S. A. Abel, M. D. Goodsell, J. Jaeckel, V. V. Khoze, and A. Ringwald. arXiv:0803.1449 [hep-ph].
3. L. B. Okun. *Sov. Phys. JETP* **56** (1982) 502.
4. V. V. Popov and O. V. Vasil'ev. *Europhys. Lett.* **15** (1991) no. 1, 7–10; V. Popov. *Turkish Journal of Physics* **23** (05, 1999) 943–950.
5. D. F. Bartlett and S. Loegl. *Phys. Rev. Lett.* **61** (1988) 2285–2287; E. R. Williams, J. E. Faller, and H. A. Hill. *Phys. Rev. Lett.* **26** (1971) 721–724.
6. G. G. Raffelt and D. S. P. Dearborn. *Phys. Rev.* **D36** (1987) 2211.
7. J. Redondo. arXiv:0801.1527 [hep-ph].
8. **CAST collaboration** Collaboration, K. Zioutas. *et al. Phys. Rev. Lett.* **94** (2005) 121301, hep-ex/0411033; *JCAP* **0704** (2007) 010, hep-ex/0702006.
9. K. van Bibber, P. M. McIntyre, D. E. Morris, and G. G. Raffelt. *Phys. Rev.* **D39** (1989) 2089.
10. S. N. Gninenko and J. Redondo. arXiv:0804.3736 [hep-ex].
11. J. Jaeckel, J. Redondo, and A. Ringwald. arXiv:0804.4157 [astro-ph].
12. K. Ichikawa. arXiv:0706.3465 [astro-ph]; U. Seljak, A. Slosar, and P. McDonald. *JCAP* **0610** (2006) 014, arXiv:astro-ph/0604335; M. Cirelli and A. Strumia. *JCAP* **0612** (2006) 013, arXiv:astro-ph/0607086.
13. J. Hamann, S. Hannestad, G. G. Raffelt, and Y. Y. Y. Wong. *JCAP* **0708** (2007) 021, arXiv:0705.0440 [astro-ph].
14. **ALPS** Collaboration, K. Ehret *et al.* hep-ex/0702023. See http://alps.desy.de/.
15. P. Sikivie. *Phys. Rev. Lett.* **51** (1983) 1415. [Erratum-ibid. **52**, 695 (1984)].
16. **BRFT** Collaboration, R. Cameron *et al. Phys. Rev.* **D47** (1993) 3707–3725.
17. **GammeV (T-969)** Collaboration, A. S. Chou *et al. Phys. Rev. Lett.* **100** (2008) 080402, arXiv:0710.3783 [hep-ex].
18. **BMV** Collaboration, C. Robilliard *et al. Phys. Rev. Lett.* **99** (2007) 190403, arXiv:0707.1296 [hep-ex].
19. **PVLAS** Collaboration, E. Zavattini *et al. Phys. Rev. Lett.* **96** (2006) 110406, hep-ex/0507107. *Phys. Rev.* **D77** (2008) 032006, arXiv:0706.3419 [hep-ex].
20. M. Ahlers, H. Gies, J. Jaeckel, J. Redondo, and A. Ringwald. *Phys. Rev.* **D77** (2008) 095001, arXiv:0711.4991 [hep-ph].
21. J. Jaeckel and A. Ringwald. *Phys. Lett.* **B653** (2007) 167–172, arXiv:0706.0693 [hep-ph].
22. J. Jaeckel and A. Ringwald. *Phys. Lett.* **B659** (2008) 509–514, arXiv:0707.2063 [hep-ph].
23. **Particle Data Group** Collaboration, W. M. Yao *et al. J. Phys.* **G33** (2006) 1–1232.
24. P. Langacker and N. Polonsky. *Phys. Rev.* **D52** (1995) 3081–3086, arXiv:hep-ph/9503214.
25. W. de Boer and C. Sander, Phys. Lett. B **585**, 276 (2004) [arXiv:hep-ph/0307049].
26. A. Ibarra, J. Redondo, A. Ringwald and C. Weniger. In preparation.

DM-TPC: A DARK MATTER TIME PROJECTION CHAMBER

Steven Ahlen
for the DM-TPC Collaboration[a],
Physics Department, Boston University, Boston, Massachusetts, USA 02215

The DM-TPC collaboration is developing an optical read-out time projection chamber for dark matter detection and identification. The detection material is low pressure CF4 gas, which has exceptional characteristics making it highly suitable for this purpose. Among these are excellent electron diffusion and scintillation performance, and the great sensitivity of fluorine to spin-dependent dark matter interactions. A summary of progress of the research and development program will be presented here.

1 An Imaging Time Projection Chamber

The concept of the Dark Matter Time Projection Chamber (DM-TPC) is illustrated in figure 1. The chamber contains CF4 gas at low pressure. An incoming dark matter particle collides elastically with an F nucleus, causing it to recoil with 10 to 100 keV of energy, with a range the order of one mm or more. The ionization electrons drift to the readout plane, where an electron avalanche occurs, accompanied by the emission of copious amounts of scintillation light. The scintillation light is imaged by the lens and CCD camera. Information on the component of the track perpendicular to the plane is provided by the time profile of a PMT signal recorded with a waveform digitizer. CF4 is an ideal gas due to its large scintillation efficiency and excellent electron diffusion characteristics. Furthermore, F has excellent properties for use in searches for dark matter through spin dependent interactions.
We have built two prototype detectors that have demonstrated this technique. An MIT prototype has used a readout plane consisting of a Multi-Wire-Proportional-Chamber (MWPC) to

[a] *DM-TPC Collaboration: S. Ahlen, D. Avery, H. Tomita, A. Roccaro, K.Otis, M. Lewandowska (Boston University); N. Skvorodnev, H. Wellenstein (Brandeis University); and B. Cornell, D. Dujmic, W. Fedus, P. Fisher, S. Henderson, A. Kaboth, J. Monroe, T. Sahin, G. Sciolla, R. Vanderspek, R. Yamamoto, H. Yegoryan (MIT)

show that the direction of recoiling F nuclei can be determined. Examples of recoil tracks are shown in figure 2 for a CF4 pressure of 200 torr [1]. The recoils were produced by elastic collisions with neutrons, and extend down to energies of about 200 keV. Since the stopping power decreases as a particle's velocity approaches zero, the stopping end of the track is the one with reduced light yield. We expect that this effect will be observable below 100 keV when operated at lower pressure. Furthermore, we have recently developed a mesh readout plane that will also help with this goal. Tracks using the mesh in the MIT prototype are shown in figure 3. The stainless steel mesh, with wire diameter 30 μm and wire pitch 320 μm, was supported over a copper plate with spacers made of 300 μm plastic foil. With a CF4 pressure of 200 torr, the mesh operated with 2000 volts between the mesh and copper plate without sparking. The tracks shown in Figure 3 were produced by alpha particles. The Bragg peak from one alpha track is shown in figure 4. A second prototype has recently built at Boston University. This device has a 25 cm by 25 cm mesh and a cylindrical field cage 25 cm in diameter and 25 cm high.

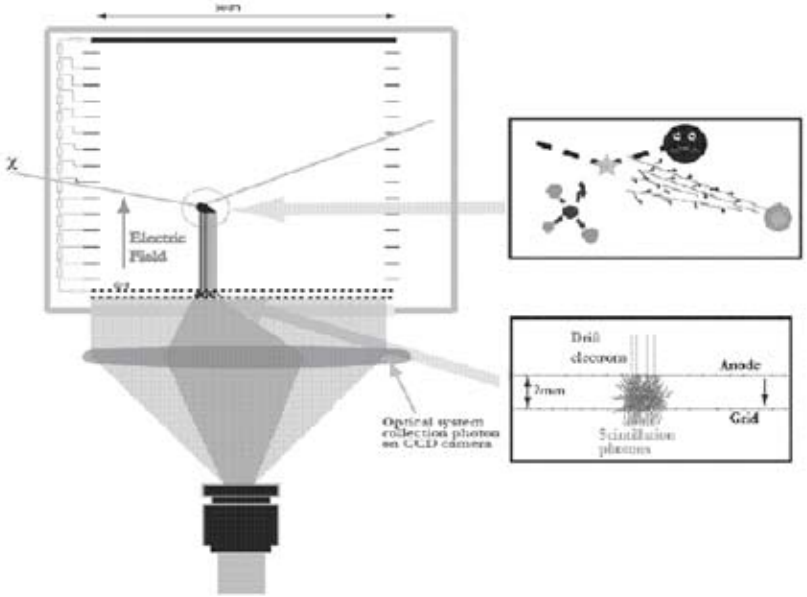

Figure 1: Schematic of DM-TPC.

2 Dark Matter Search via Spin-Dependent Interactions: Majorana Neutrinos

The latest cosmic microwave background results show that the matter content of the universe is 5.7 times larger than exists in the form of ordinary baryonic material [2]. Through observations of visible light, x-rays, and weak gravitational lensing of the collision of two clusters of galaxies, the dark matter has been found to interact very weakly, if at all, with itself and with ordinary matter by any means other than gravitation [3]. Many hypothetical particles have been advanced as candidates for dark matter. The list includes axions, the neutralino from supersymmetry, technibaryons, and massive fourth generation neutrinos from many models. Data on neutrino oscillations and direct limits on the mass of the electron neutrino from beta decay experiments have shown that the neutrinos from the first three generations are too light to provide the cold dark matter required for galaxy formation. LEP excludes fourth generation neutrinos with mass less than half the Z mass, and the first direct search for dark matter excluded massive Dirac neutrinos as the dark matter of our Galaxy for neutrino masses between 20 GeV and 2 TeV [4].

Massive Majorana neutrinos have not yet been excluded as the dark matter. We consider the search for these particles to illustrate the potential of the DM-TPC.

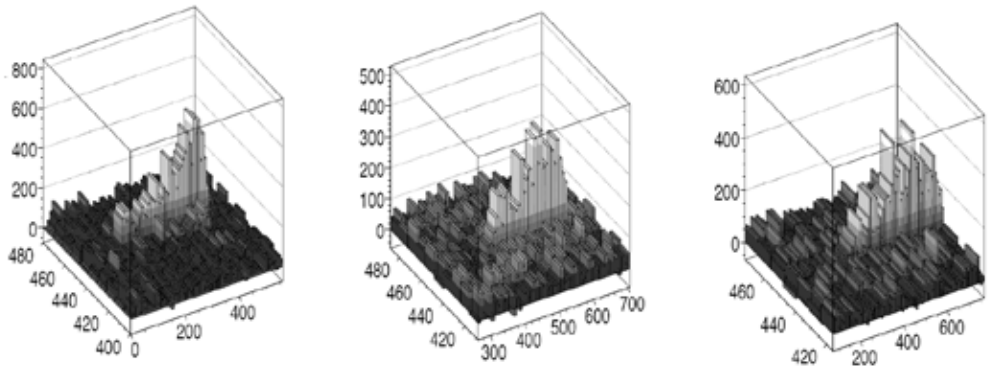

Figure 2: Tracks of recoiling F nuclei from collisions with neutrons. The neutrons came from the right. The direction of the neutron can be inferred from the track.

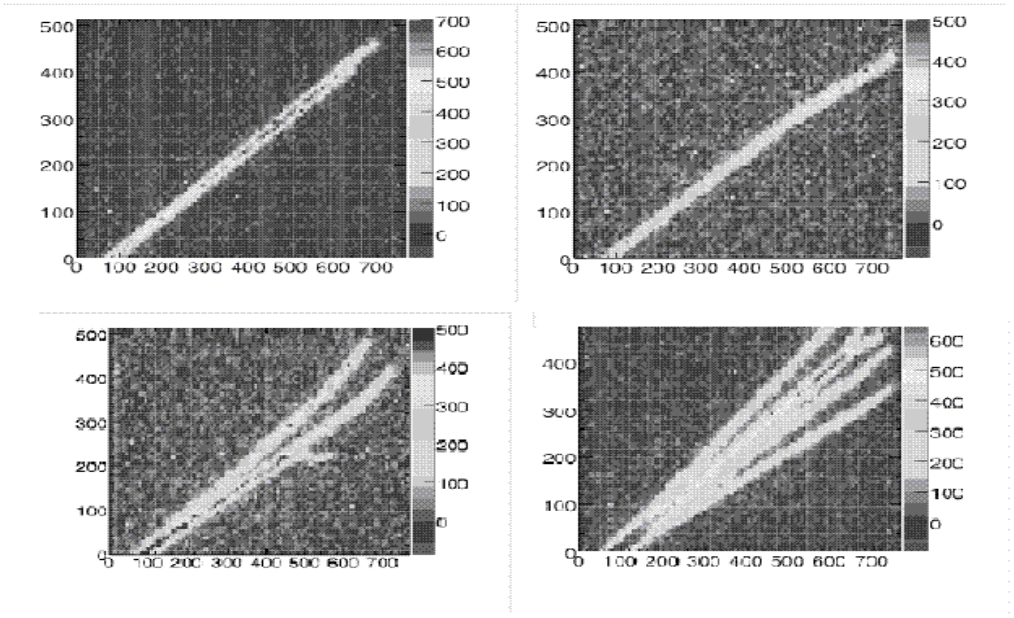

Figure 3: Alpha tracks from MIT prototype using mesh readout plane

Majorana neutrinos are predicted by numerous theories. They have been shown to be viable as dark matter in a minimal technicolor theory [5]. The authors of reference 5 have shown that the relic density of Majorana neutrinos can be in the observationally determined range if the Universe has a nonstandard history including an early dominance by a rolling scalar field as predicted by many models for dynamical dark energy. Majorana neutrinos also show up as Kaluza-Klein particles in a theory involving the universal extra dimension scenario [6]. Their collision cross section with nuclei is determined by their mass and the properties of the nuclei they interact with. The total cross section is $\sigma = \frac{2G_F^2\mu^2}{\pi\hbar^4}C^2\lambda^2 J(J+1)$, where μ is the reduced mass of the neutrino, J is the nuclear angular momentum quantum number of the nucleus, and $\lambda^2 J(J+1)$

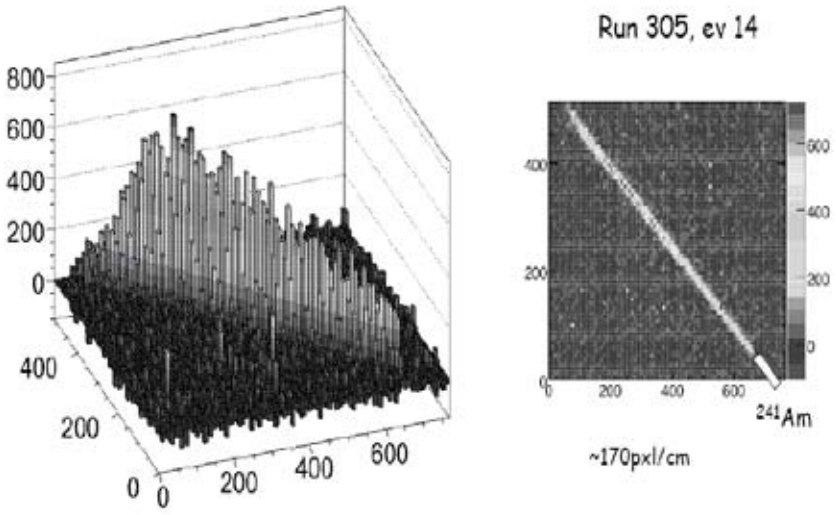

Figure 4: Bragg peak from alpha track using MIT prototype with mesh.

is the "spin-factor" of the nucleus. C is related to the quark spin content of the unpaired nucleon [7] and is 0.68 for the proton and -0.58 for the neutron. Estimates of the nuclear spin factor are given in reference 7 for a number of isotopes. The product of squared nucleus mass, isotopes per kg, and nuclear spin factor is a figure of merit as a Majorana neutrino detecting medium. This figure of merit is listed in parentheses (arbitrary units) for various promising nuclides: 1H (4.48), 19F (74.05), 23Na (5.68), 27Al (14.16), 43Ca (0.06), 73Ge (2.24), 93Nb (90.85), 127I (5.36), 129Xe (25.00), 131Xe (9.18). Form factor effects are difficult to calculate for spin-dependent interactions, but for F the effect [7] is less than 20% for recoil energies less than 100 keV. Thus it is seen that F provides the best return per kg of detector mass as any other detecting material. Leaving out the form factor correction term and assuming the neutrino mass is large compared to the F mass, the cross section for a Majorana neutrino with a fluorine nucleus is 3.1 pb. For a local dark matter density of 0.4 GeV/cm^3 there would be 300 interactions per year for 100 GeV neutrino mass in 1 kg of F. A few dozen of these would likely have recoil kinetic energies in excess of 100 keV, when one includes the effects of the tails of the neutrino velocity distribution. With our direction sensitive detector we can use the measured directions of the high energy recoils to test the hypothesis that they are produced in collisions with particles coming from the direction of the constellation Cygnus, which is believed to be the case for dark matter particles.

In the next year we plan to build a detector with a mass of 70 g of fluorine in a volume of 0.1 m^3 of CF4 at a gas pressure of 150 torr. The device will be operated at an appropriate underground site to reduce backgrounds from neutrons. The detector will have in a single vacuum vessel four cells, each of the order of 30 cm on a side based on diffusion and optical considerations. Each cell will be viewed by one CCD camera and two PMTs. This will permit 3-D track reconstruction and redundancy will enable the elimination of background events due to radioactivity events in the CCDs. The device would detect about one Majorana neutrino interaction per month if these particles are the dark matter.

References

1. D. Dujmic et al., Nucl. Instr. Meth. Phys. Res. A, 584, 327 (2008)

2. D.N. Spergel et al., Ap.J. Supp. 170, 377 (2007).
3. D. Clowe et al., Ap.J. Lett. 648, L109 (2006).
4. S.P. Ahlen et al., Phys. Lett. 195B, 603 (1987).
5. K. Kainulainen et al., Phys. Rev. D 75, 085003 (2007).
6. V.K. Oikonomou et al., Nucl. Phys. B 773, 19 (2007).
7. J.D. Lewin and P.F. Smith, Astroparticle Physics 6, 87 (1996).

Cosmic Rays

THE AIR-FLUORESCENCE YIELD

F. Arqueros, F. Blanco, D. Garcia-Pinto, M. Ortiz and J. Rosado
Departmento de Fisica Atomica, Molecular y Nuclear, Facultad de Ciencias Fisicas, Universidad Complutense de Madrid, Madrid 28040, Spain

Detection of the air-fluorescence radiation induced by the charged particles of extensive air showers is a well-established technique for the study of ultra-high energy cosmic rays. Fluorescence telescopes provide a nearly calorimetric measure of the primary energy. Presently the main source of systematic uncertainties comes from our limited accuracy in the fluorescence yield, that is, the number of fluorescence photons emitted per unit of energy deposited in the atmosphere by the shower particles. In this paper the current status of our knowledge on the fluorescence yield both experimental an theoretical will be discussed.

1 Introduction

Fluorescence telescopes have been successfully used for the detection of ultra-high energy cosmic rays ($> 10^{18}$ eV) since the pioneering Fly's Eye experiment [1]. In this technique the fluorescence radiation induced by the charged particles of the extensive air shower generated by a primary cosmic ray is registered at ground by wide-angle telescopes. Assuming that the intensity of the air-fluorescence light is proportional to the energy deposited in the atmosphere by the shower, this technique provides a nearly calorimetric measure of the energy of the primary cosmic ray. Therefore it has the advantage, as compared with methods relying on simulations (e.g. surface arrays working in standalone mode), of being nearly model independent. In spite of this advantage, fluorescence telescopes are presently limited by the uncertainty in the fluorescence yield, that is, the calibration parameter which converts number of fluorescence photons into absolute energy units. For instance in the Pierre Auger Observatory [2] the uncertainty in the fluorescence yield contributes a 14% to the total systematic error in the energy calibration which is presently 22%.

In order to improve the accuracy of this parameter, dedicated laboratory experiments [3] are carrying out precise measurements of the air-fluorescence emission. In these experiments an

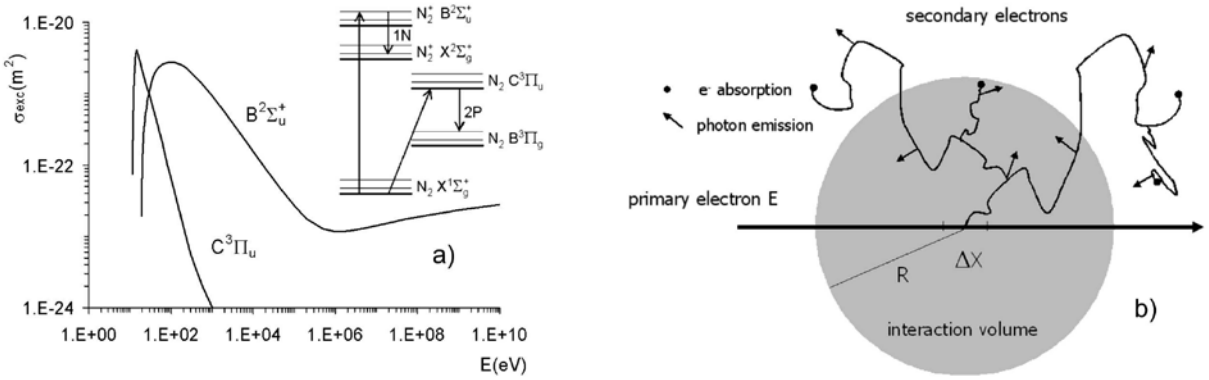

Figure 1: a) Molecular levels of N_2 and N_2^+ involved in the generation of air-fluorescence and cross section versus electron energy for the excitation of the corresponding upper levels. b) At high electron energy most of the fluorescence light is generated by secondary electrons.

electron beam excites air at certain pressure and temperature conditions. A large set of experimental parameters are measured, not only the absolute value of the fluorescence yield but also the spectral features of the fluorescence radiation and the dependence with atmospheric parameters (pressure, temperature, humidity, etc.). On the other hand, progress on the theoretical understanding of the various processes leading to the air-fluorescence emission is being carried out [4].

2 The generation of air fluorescence excited by electrons

2.1 Physical processes

Air-fluorescence in the near UV range (300 - 400 nm) is basically produced by the de-excitation of atmospheric nitrogen molecules excited by the shower electrons. Most of the fluorescence light comes from the 2P System of N_2 and the 1N System of N_2^+ (Fig. 1a). Excited molecules can also decay by collisions with other molecules (collisional quenching). This effect which grows with pressure P, reduces the fluorescence intensity by a factor $1 + P/P'_\lambda$. The characteristic pressure P'_λ is defined, for a given $v - v'$ band of wavelength λ, as the one for which collisional quenching and radiative decay have the same probability.

Basically two different parameters are being used for the energy calibration of fluorescence telescopes. The first one ε_λ is the number of photons of a given molecular band emitted per electron and unit path length, $\varepsilon_\lambda = N \times \sigma_\lambda/(1 + P/P'_\lambda)$, where N is the density of nitrogen molecules and σ_λ is the cross section for the excitation of the molecular band. The second parameter is the *fluorescence yield* Y_λ, defined as the number of photons emitted per unit deposited energy.

$$Y_\lambda = Y_\lambda^0 \frac{1}{1 + P/P'_\lambda}\,, \qquad Y_\lambda^0 = \frac{A_\lambda}{(\mathrm{d}E/\mathrm{d}X)_{dep}}\,. \tag{1}$$

Y_λ^0 is the fluorescence yield in the absence of quenching. A_λ and $(\mathrm{d}E/\mathrm{d}X)_{dep}$ are respectively the number of emitted photons at zero pressure and the deposited energy both per unit mass thickness. The fluorescence yield as defined in (1) is more useful for calorimetric applications. Notice that for the determination of Y_λ, both photon number and deposited energy has to be measured in the same volume. This is particularly important for laboratory experiments carried out in small gas chambers. In this case secondary electrons ejected in ionization processes might escape the field of view of the optical system before depositing all the energy (Fig. 1b). In next section the role of secondary electrons in the generation of air-fluorescence light is described.

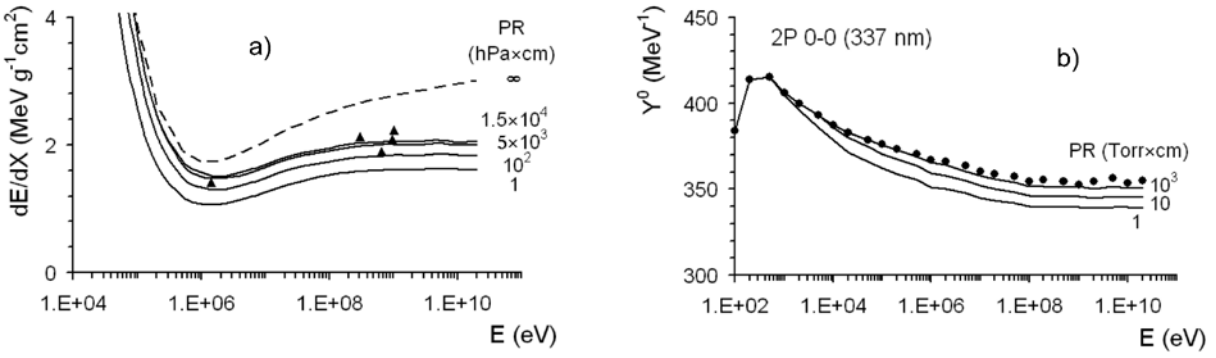

Figure 2: a) Continuous lines represent the energy deposited per unit mass thickness versus electron energy for several values of PR. Dashed line is the total energy loss of the electron. Triangles represent the relative values of the air-fluorescence yield measured by Kakimoto *et al.* b) Fluorescence yield at zero pressure versus primary energy for the 337 nm band.

2.2 Secondary electrons

Secondary electrons from ionization processes are the main source of fluorescence light, since the excitation cross sections show a fast decrease with energy (Fig. 1a), in particular the one for the 2P system. A high energy electron loses energy as a result of collisions with air molecules. Ionization processes give rise to the ejection of secondary electrons which deposit their energy within a certain distance from the interaction point (Fig. 1b). The average energy deposited per unit mass thickness inside a given volume around the interaction point can be expressed as

$$\rho\frac{\mathrm{d}E_{dep}}{\mathrm{d}X} = N_{air}\{< E^0_{dep} > + < E_{dep} >\}\sigma_{ion}(E)\,, \quad < E^0_{dep} >=< E_{exc} > \frac{\sigma_{exc}}{\sigma_{ion}} + I + < E^{ion}_{exc} >\,, \tag{2}$$

where ρ is the air density, N_{air} is the number of air molecules per unit volume and σ_{ion} is the ionization cross section. The average energy deposited in the medium by the primary electron per primary ionization process $< E^0_{dep} >$ is obtained from several molecular parameters [a]. The energy deposited in the volume by the secondary electrons $< E_{dep} >$ is calculated by a dedicated simulation [4]. Figure 2a) shows the result for a sphere of radius R (Fig. 1b). As expected, the deposited energy depends on PR and for an unlimited medium, $PR \to \infty$, equals the energy loss predicted by the Bethe-Bloch theory.

Neglecting the collisional quenching, the number of photons emitted per electron and per unit path length can be expressed by $\varepsilon_\lambda(P) = \rho A_\lambda = N\{\sigma_\lambda(E) + \alpha_\lambda(E,P)\sigma_{ion}(E)\}$, where $\alpha_\lambda(E,P)$ is the average number of photons generated inside the volume per secondary electron, also calculated in the simulation. A very simple expression for Y^0_λ can be obtained from the above equations

$$Y^0_\lambda = \frac{N}{N_{air}} \times \frac{\frac{\sigma_\lambda}{\sigma_{ion}} + \alpha_\lambda}{< E^0_{dep} > + < E_{dep} >}\,, \tag{3}$$

This procedure allows theoretical predictions on the absolute value of Y^0_λ and its dependence on the electron energy as shown below.

2.3 Fluorescence emission versus deposited energy

The energy calibration of fluorescence telescopes relies on the assumption that the intensity of fluorescence light is proportional to the energy deposited in the atmosphere, that is, the

[a] ionization potential I, total excitation cross section σ_{exc}, average excitation energy of neutral molecules $< E_{exc} >$ and of ionized molecules $< E^{ion}_{exc} >$.

fluorescence yield is assumed to be independent on the electrons energy. The validity of this assumption can be theoretically checked by means of the model described above. Fig. 2b) shows Y^0 versus E for the most intense band of the 2P system (0-0 transition at 337 nm). The results shown in this plot can be summarized as follows. The fluorescence yield decreases with E about a 10% in the range 1 keV - 1 MeV and about 4% in the interval 1 MeV - 20 GeV. This smooth dependence of the fluorescence yield on E has no impact on the energy calibration of fluorescence telescopes. The proportionality assumption has been also verified experimentally by several groups [5].

3 The dependence of the fluorescence yield on atmospheric parameters

Fluorescence yield depends on pressure, temperature T and humidity. Thus for a precise energy calibration of fluorescence telescopes these dependencies have to be determined accurately.

As mentioned above collisional quenching reduces the fluorescence emission by a factor $1 + P/P'_\lambda$. In the general case, for a mixture of gases (e.g. nitrogen, oxygen, water vapor, etc.), the characteristic pressure obeys the law

$$\frac{1}{P'} = \sum_i \frac{f_i}{P'_i}\,, \qquad P'_i = \frac{kT}{\tau}\frac{1}{\sigma_{Ni}\bar{v}_{Ni}}\,, \qquad \bar{v}_{Ni} = \sqrt{\frac{8kT}{\pi\mu_{Ni}}}\,, \tag{4}$$

where f_i is the fraction of molecules of type i in the mixture, σ_{Ni} is the collisional cross section which depends on the particular band, and v_{Ni} and μ_{Ni} are the relative velocity and reduced mass of the two body system N-i respectively.

The experimental procedure for the determination of the dependence of fluorescence yield on the above parameters is the following. At a fixed temperature the dependence of fluorescence intensity on pressure is measured for dry air. This measure, if properly carried out [b], allows a determination of P' and therefore the dependence of the fluorescence yield on pressure at a fixed temperature. Experimental values of P' for the molecular bands of the 2P and 1N systems in dry air at room temperature have been reported by many authors [3]. The most complete set of P' values have been reported very recently by AIRFLY [6] improving the accuracy of previous measurements. This set of values are being used by the Pierre Auger Observatory [2] for the calculation of the dependence of the fluorescence yield versus altitude [c].

The P' parameter depends on temperature because the collision frequency grows with $\sqrt{T}$ as predicted by the kinetic theory of gases. In addition the collisional cross section depends on the kinetic energy of the encounters following a power law ($\sim T^\alpha$). Assuming this effect is negligible, the temperature dependence of the fluorescence yield can be easily predicted by equation (4). Recently some experimental works [5] have found a noticeable variation of the collisional cross section with temperature. According to the preliminary values reported by AIRFLY [7], neglecting this effect results in an overestimation of the fluorescence yield by an amount going up to $\approx$ 20% for the 1N (0-0) 391 nm band.

Water molecules have a significant cross section for the air-fluorescence quenching and therefore humidity modifies the value of P'. Several authors [5] have measured the dependence of fluorescence intensity on humidity. A decrease of the fluorescence yield up to a 20% is found (at 100% relative humidity). From these measurements, values of the characteristic pressure for the quenching with water molecules P'_{H_2O} have been determined for the main molecular bands of nitrogen.

[b] the effect of secondary electrons escaping the field of view might introduce systematic errors.

[c] the contribution of the pressure dependence to the total uncertainty in the energy determination has been reduced to a 1%.

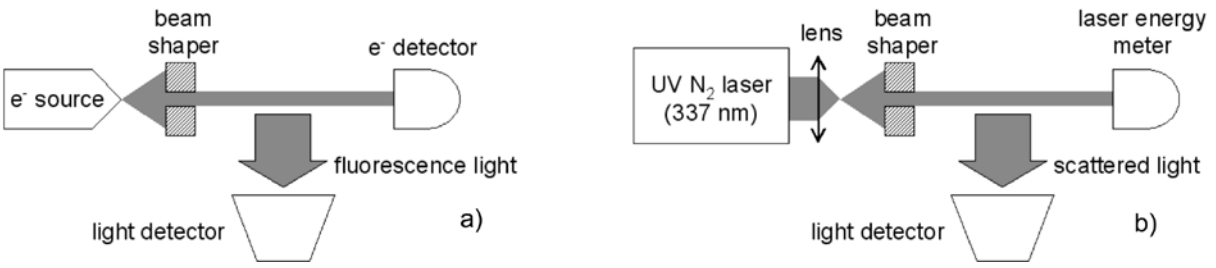

Figure 3: Comparison of fluorescence signal generated by a) an electron beam with b) that from Rayleigh scattering of a nitrogen laser. This procedure allows the absolute calibration of the optical system.

4 Absolute value

The accurate measurement of the absolute value of the fluorescence yield is an experimental challenge. The value is obtained as the ratio $Y_\lambda = N_\lambda/(N_e \times EDEP)$. For the measurement of the absolute number of fluorescence photons in the wavelength interval of interest N_λ, the efficiency of the various elements of the collection and detection system has to be known accurately. The number of electrons traversing the observation region N_e has to be absolutely measured as well. Finally the total energy $EDEP$ deposited in the volume from where the registered fluorescence was emitted has to be determined (usually by means of a Monte Carlo simulation). In order to reduce systematic errors in the optical calibration (e.g. PMT quantum efficiency, transmission of optical elements, geometrical factors, etc.) some techniques have been developed, based on the comparison with well known physical processes like Cherenkov emission or Rayleigh scattering (Fig. 3).

Several measurements of Y_λ are presently available [3]. Unfortunately the comparison is not simple since some authors report the experimental result of ε_λ (i.e. photons/m) while others provide Y_λ (i.e. photons/MeV). In addition the spectral intervals of the various experiments use to be different. A detailed summary of the available results can be found elsewhere[5]. Here we will compare some representative experimental data (Tab. 1). For this comparison, measured values of ε_λ are converted into fluorescence yields using our results on deposited energy. Notice that deposited energy is weakly dependent on the size of the region and therefore a rough estimate of the equivalent R value is sufficient. From these results the fluorescence yield Y_{337} for the most intense band, 2P (0-0) at 337 nm, is calculated using the experimental relative intensities reported by AIRFLY [6]. Finally the Y_{337} values have been normalized to 293 K temperature and 1013 hPa pressure using equations (1) and (4). This procedure is appropriate for a comparison of measurements with typical uncertainties of about 13% or higher. Results are shown in last column of Tab. 1.

Firstly, the ε_λ values of Kakimoto *et al.* in the range 300-400 nm at several energies have been superimposed in Fig. 2a) to the energy deposited at atmospheric pressure assuming an observation volume with R ranging between 5 and 15 cm. The comparison of fluorescence intensity (photons/m) with deposited energy has allowed the determination of the fluorescence yield (photons/MeV) in that wavelength interval.

The ε_{337} value of 1.021 photons/m from Nagano *et al.* has been combined with the deposited energy for $R \approx 5$ cm giving the corresponding Y_{337} value. For the determination of the fluorescence yield, both MACFLY and FLASH calculate the deposited energy from a MC simulation. For these experiments only the conversion for wavelength intervals as well as minor T and P corrections were necessary. Finally AIRFLY reports a preliminary value of Y_{337} determined from the ratio of the absolute number of photons and the energy deposited according to a GEANT4 simulation.

Table 1: Comparison of data on fluorescence yields. Experimental results are used to infer the value of the fluorescence yield for the 337 nm band at $T = 293$ K and $P = 1013$ hPa (last column). See text for details.

Experiment	$\Delta\lambda$ nm	T [K]	P [hPa]	experimental result	$I_{337}/I_{\Delta\lambda}$	Y_{337} $[\mathrm{MeV}]^{-1}$
Kakimoto *et al.*	300 - 400	288	1013	see text	0.278	5.4
Nagano *et al.*	337	293	1013	1.021 ph./m	1	5.5
MACFLY	290 - 440	296	1013	17.6 ph./MeV	0.261	4.6
FLASH 07	300 - 420	304	1013	20.8 ph./MeV	0.276	5.6
AIRFLY (prelim.)	337	291	993	4.12 ph./MeV	1	4.0

5 Conclusions

Our understanding on the processes leading to generation of air fluorescence has increased significantly in the last years [5]. The world-wide campaign for the experimental determination of the fluorescence yield has achieved remarkable results, in particular in the measurement of the various dependencies with atmospheric parameters. The fundamental assumption of proportionality between fluorescence intensity and deposited energy has been verified both theoretically and experimentally.

In regard with the determination of the absolute value of the fluorescence yield new data are available. However the interpretation of the results is not straightforward. A comparison using the procedure discussed here shows a general agreement with typical differences of about 15%. For a real improvement in the accuracy of fluorescence telescopes an uncertainty better than 10% in the fluorescence yield is necessary. Several experiments claim high accuracy, for instance, the reported uncertainty of the FLASH experiment is of about 8%. In addition the AIRFLY collaboration will publish soon a final absolute value with an error below 10%. A discussion on these and other high accuracy measurements have been presented elsewhere [5]. Discrepancies between these experiments go beyond the reported accuracies and therefore some experimental effort is still necessary to clarify the situation.

Acknowledgments

This work has been supported by the Spanish MEyC (Ref.: FPA2006-12184-C02-01), CONSOLIDER - INGENIO2010 program CPAN (CSD2007-000042) and CM-UCM (Ref.: 910600).

References

1. R.M. Baltrusaitis *et al.*, *Nucl. Instr. and Meth.* A **240**, 410 (1985).
2. J. Abraham *et al.* (Pierre Auger Collaboration), Phys. Rev. Lett. (submitted).
3. F. Kakimoto *et al.*, *Nucl. Instr. and Meth.* A **372**, 527 (1996); M. Nagano *et al.*, *Astropart. Phys.* **22**, 235 (2004); R. Abbasi *et al.*, *Astroparticle Physics* **29**, 77 (2008); P. Colin *et al.* (MACFLY Coll.), *Astropart. Phys.* **27**, 317 (2007).
4. F. Blanco, F. Arqueros, *Phys. Lett A* **345**, 355 (2005); F. Arqueros *et al.*, *Astropart. Phys.* **26**, 231 (2006); F. Arqueros *et al.*, arXiv:0712.3536, *Proc. 5th Fluorescence Workshop* (El Escorial, Madrid, Spain 2007) to appear in *Nucl. Instr. and Meth. A.*
5. F. Arqueros *et al.*, *Summary of the 5th Fluorescence Workshop* in *Proc. 5th Fluorescence Workshop* (El Escorial, Madrid, Spain 2007); to appear in *Nucl. Instr. and Meth. A.*
6. M. Ave *et al.* (AIRFLY Coll.), *Astropart. Phys.* **28**, 41 (2007).
7. M. Ave *et al.* (AIRFLY Coll.), arXiv:0711.4583, *Proc. 5th Fluorescence Workshop* (El Escorial, Madrid, Spain 2007); to appear in *Nucl. Instr. and Meth. A.*

THE FLUX AND THE COMPOSITION OF ULTRA HIGH ENERGY COSMIC RAYS MEASURED BY THE PIERRE AUGER OBSERVATORY

I. C. MARIŞ for the Pierre Auger Collaboration
Institut für Experimentelle Kernphysik, Universität Karlsruhe (TH), Postfach 6980, 76128 Karlsruhe

The cosmic ray flux above 10^{18} eV has been measured with high statistics by the Pierre Auger Observatory. At high energies the flux is suppressed and the hypothesis of a single power-law behavior as obtained in the lower energy range is rejected with a significance of more than 6 sigma. The measurement of the shape of the energy spectrum of ultra high energy cosmic rays can constrain acceleration models only when combined with a composition determination. The fluorescence detector measurement of the longitudinal development of air showers is used to determine the cosmic ray composition and the surface detector data are used to derive upper limits on the flux of photons and tau neutrinos.

Introduction

In the near future the wealth of data recorded by the Pierre Auger Observatory will help to answer some of the main questions in ultra high energy cosmic ray (UHECR) physics, such as their origin and composition. Due to the Greisen-Zatsepin-Kuzmin effect (GZK) [1,2] a flux suppression is expected in the highest energy range, mainly caused by the energy loss of cosmic rays interacting with the microwave background radiation. This has been seen both by the Pierre Auger Observatory [3] and by the HiRes collaboration [4]. Through the hybrid technique of observing the same air showers with two different detectors, the nearly calorimetric estimation of the energy of the primary particle as obtained from the fluorescence technique is transfered to the large number of events recorded by the surface detector. This method is described below in section 1 and the resulting energy spectrum in section 2.

The excess of cosmic rays above the energy threshold given by the GZK effect, as reported by the AGASA experiment [5] might be explained in the so-called *top down* models. In some of these scenarios the origin of cosmic rays is at relatively close distances to the Earth and therefore

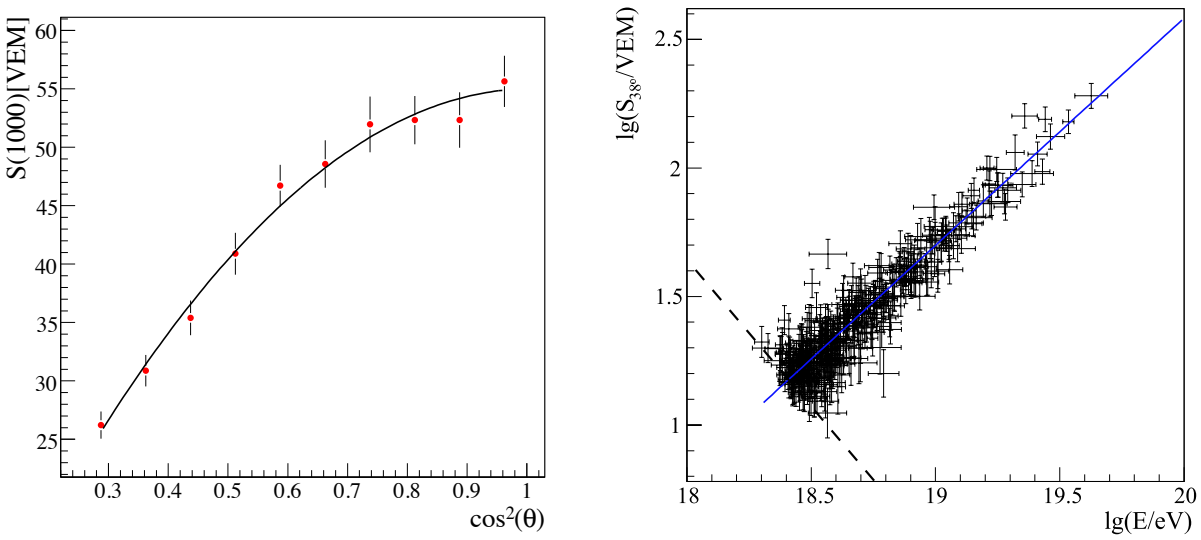

Figure 1: (left hand side) S(1000) attenuation in the atmosphere. The line represents an empirical fit that is used for the conversion to S_{38}. (right hand side) Energy calibration. The events at low energies (below the dashed line) have been rejected to avoid threshold effects. The relation between S_{38} and energy is almost linear and is shown with the continuous line [3].

a large photon content in the cosmic ray flux is predicted at the highest energies. Limits on photon content are presented in section 3 below.

1 Energy calibration

The Pierre Auger Observatory, located in the province of Mendoza (Argentina), is used to measure the properties of extensive air showers by observing their longitudinal development in the atmosphere as well as their lateral spread at ground level. The Observatory consists of 1600 water-Cherenkov detectors(SD), filled with 12 tonnes of water each and equipped with three photomultipliers to detect secondary photons and charged particles. The tanks are spread over 3000 km^2 on a triangular grid of 1.5 km spacing. The atmosphere above the array is viewed by 4 fluorescence detectors (FD), each housing 6 telescopes, located on the border of the area. The field of view of each telescope is 30° in azimuth, and $1.5-30°$ in elevation. Light is focused with a spherical mirror of 11 m^2 effective area on a camera of 440 hexagonal pixels. Each pixel is a photomultiplier tube with 18 cm^2 detection area. More details on detector setup and calibration can be found in [6,7].

After entering the atmosphere, cosmic rays interact with nuclei in the air and start creating extensive air showers. The muons, electrons and photons that reach the ground are detected with the SD, their lateral spread from the air shower axis at primary energies above 10^{18} eV being in the order of a few kilometers. On the way through the atmosphere charged particles excite nitrogen molecules, which afterwards emit fluorescence light in the ultra-violet band. The amount of light is proportional to the energy deposited by the air shower in the atmosphere and is detected with the FD.

The SD has a high duty cycle of almost 100 %, but the energy calibration can be inferred in a model-independent way only from the FD energy assignment [8]. The detected signal at 1000 m from the shower axis on the ground level, S(1000), is a good estimator for the energy of the cosmic ray. Due to the attenuation in the atmosphere, S(1000) depends on the zenith angle: an air shower developing vertically produces a smaller signal than an inclined shower produced by

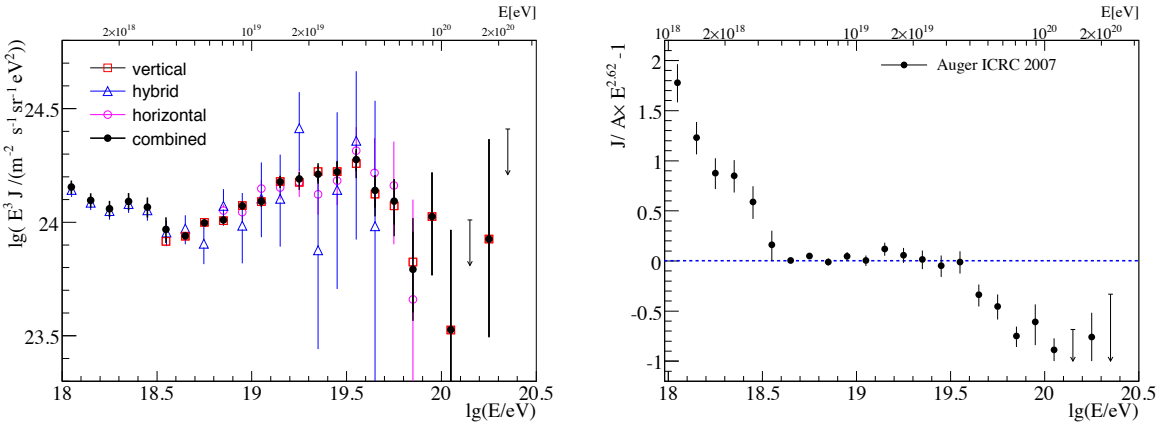

Figure 2: (left hand side) Flux multiplied by E^3 derived from hybrid data set (opened triangles) together with the spectra obtained from the SD using showers with zenith angles of less than 60° (opened squares) and more than 60° (opened circles). The Auger combined energy spectrum is denoted by filled circles. Only statistical uncertainties are shown. Arrows indicate 84% CL upper-limits. (right hand side) Fractional difference between the Auger spectrum and an assumed flux $\propto E^{-2.6}$ as a function of energy.

a cosmic ray with the same energy. The constant intensity method [3] is applied to obtain the zenith angle correction : it assumes that the cosmic ray flux is isotropic in local coordinates, i.e. the number of events above a certain threshold energy is constant as a function of $\cos^2\theta$. This hypothesis leads to the correction function for S(1000) shown in Fig. 1(left). A new variable obtained by using the empirical fit shown in the same figure, S_{38}, represents the signal at 1000 m the very same shower would have produced if it had arrived from a zenith angle of 38°. This angle corresponds to the median of the zenith angle distribution of the SD data. The number of events above a certain S_{38} is zenith angle independent. In principle the attenuation might be energy dependent, because showers with higher energies develop deeper in the atmosphere and can be observed before their maximum development. This effect was found to be negligible.

The transformation from S_{38} to energy is obtained from high quality hybrid events. These are air showers that triggered both SD and FD, so S(1000) and FD energy have been reconstructed with good accuracy. The relation between the two variables, shown in Fig. 1 (right), exhibits a power law correlation with a relative dispersion of $19 \pm 1\%$. The uncertainties in the determination of both FD energy and SD signal are assigned on event by event basis.

2 Ultra high energy cosmic ray flux

The data collected at the Pierre Auger are divided in three sets. The first set consists of air showers with zenith angle of less than 60° detected by SD. The energy calibration described above is applied in this case. The integrated exposure reported here is 5165 km^2 sr yr after some quality cuts (through February 2007), more than a factor of three larger than the exposure obtained by the largest forerunner experiment AGASA [5]. (Elsewhere in these Proceedings, Bonino reports other Auger results using an exposure through August 2007 of 9000 km^2 sr yr). The acceptance is computed by simple geometrical considerations and from the continuous monitoring of the configuration of the array [9]. The data set used for obtaining the energy spectrum contains only events with energies greater than $3 \cdot 10^{18}$ eV; above this energy the array is fully efficient.

The second set contains air showers measured by the SD with a zenith angle between 60° and 80°. The procedure to derive the energy is equivalent to the vertical events, but instead of using S_{38} the shower size is determined from the relative distributions of the two-dimensional muon number densities at ground level. The normalization factor of the muon map, N_{19}, is the estimator to be related to the hybrid energy. It gives the total number of muons relative

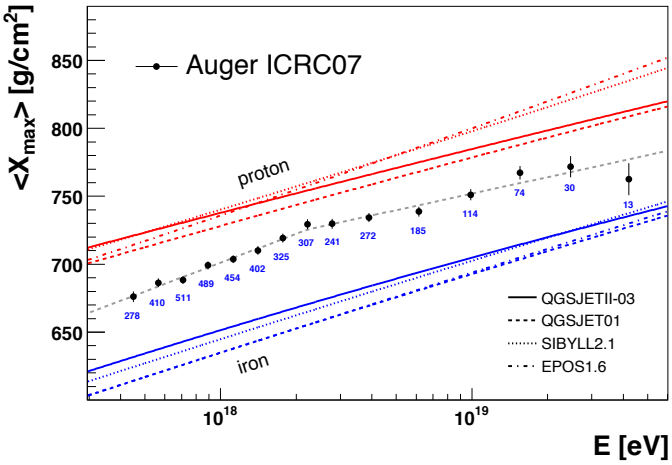

Figure 3: The mean of $X_{\max}$ distribution as a function of energy [13] together with predictions from Monte Carlo simulations. Event numbers are indicated below each data point.

to a shower initiated by a proton with an energy of 10^{19} eV. The acceptance calculation is purely geometrical and the threshold energy above which the trigger efficiency is more than 98% is $6.3 \cdot 10^{18}$ eV. Above this energy the integrated exposure until the end of February 2007 is 1510 km^2 sr yr; 29% of the equivalent acceptance for vertical events [11].

The remaining set comprises of showers detected by the fluorescence detector and at least one SD unit. The hybrid exposure calculation relies on the simulation of the FD and SD response and it is energy dependent. A large sample of Monte Carlo simulations are performed to reproduce the exact conditions of the experiment and the entire sequence of given configurations, for example the rapidly growing array, as well as the seasonal and instrumental effects. The advantage of the hybrid measurement of the energy spectrum [12] is the coverage of the energy range between 10^{18} eV and $3 \cdot 10^{18}$ eV.

The energy spectra obtained with the three methods are illustrated in Fig. 2 (left). The agreement is well within the independent systematic uncertainties, the difference between the overall normalizations is at a level of less than 4%. All spectra are affected by the 22% uncertainty in the FD energy scale, the main contributions coming from the determination of the fluorescence yield (14%), from the energy reconstruction itself (10%) and from the absolute calibration of the detector (9.5%). This systematic uncertainty does not affect the relative comparison of the three spectra. In order to obtain the Auger energy spectrum extending over the widest energy range possible, a maximum likelihood method is applied taking into account the independent uncertainties of each measurement [10]. The systematic uncertainty in the hybrid spectrum is dominated by the calculation of the exposure and reaches 20% in the low energy range. The systematic uncertainties of the SD spectra have contributions from the acceptance determination (3%) and from the conversion of S(1000) and N_{19} to energy ($< 10\%$).

In Fig. 2 (right) is illustrated the fractional difference between the Auger spectrum and a power-law $\propto E^{-2.6}$ which corresponds to the behavior of the energy spectrum between 18.6 and 19.6 in log(E/eV). Two spectral features are clearly visible: the so-called *ankle* at energies of $\approx 10^{18.5}$ eV and a flux suppression at energies above $\approx 10^{19.6}$ eV. The spectral index changes from $\gamma_1 = -3.30 \pm 0.06$ to $\gamma_2 = -2.62 \pm 0.03(\text{stat}) \pm 0.02(\text{sys})$ at $\log(E_{\text{ankle}}/\text{eV}) = 18.65 \pm 0.04$, and above $10^{19.6}$ eV to $\gamma_3 = -4.14 \pm 0.42(\text{stat})$. A continuation of the energy spectrum as a power law with index γ_2 predicts 132 ± 9 events above $10^{19.6}$ eV and 30 ± 2.5 above 10^{20} eV, whereas we observe only 51 events and 2 events. The hypothesis of a pure power-law can be rejected with a significance of 6σ.

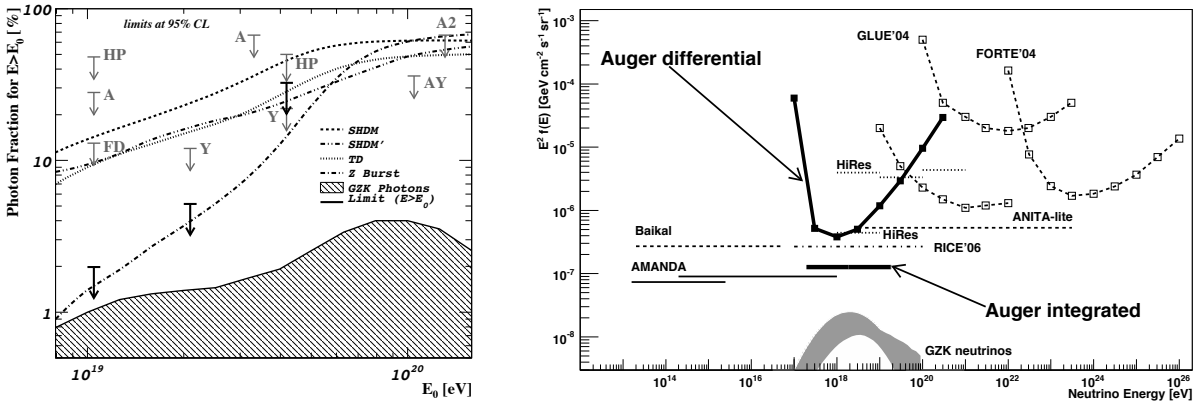

Figure 4: (left hand side) The upper limits on the fraction of photons in the integral cosmic ray flux (black arrows) along with the previous experimental limits. Also shown are the predictions from top-down models (SHDM, TD and ZB, SHDM) and with predictions of the GZK photon fraction (see [14] and ref. therein). (right hand side) Limits at 90% C.L. for a diffuse flux of ν_τ (see [15] and ref. therein).

3 Mass composition

Spectral features alone cannot constrain acceleration models. Additionally the mass of the arriving particles has to be determined. Observables related to the shower development are used to identify the nature of the primary particles. At a given energy showers from a heavier nuclei develop earlier in the atmosphere, leading to different footprints in the array or the camera.

One variable sensitive to the composition of the cosmic rays is the slant depth position $X_{\max}$ at which the maximum of the longitudinal profile occurs. Its average value is related linearly to the mean logarithmic mass, $\langle \ln A \rangle$, at a certain energy E: $\langle X_{\max} \rangle = D_p[\ln(E/E_0) - \langle \ln A \rangle] + c_p$. D_p is referred to as *elongation rate* and c_p is the average depth of a proton with energy E_0. Showers observed by at least one fluorescence detector and with at least one triggered tank were used to derive the mass composition of the cosmic rays [13]. The mean $X_{\max}$ as a function of energy together with predictions from air shower simulations is shown in Fig. 3 (left). The $X_{\max}$ uncertainty is less than $20\,\mathrm{g/cm^2}$. A moderate lightening of the primary composition is observed up to $\approx 2.5 \cdot 10^{18}\,\mathrm{eV}$, indicated by a slope larger than that of either pure proton or pure iron, whereas a constant mixed composition is present at high energies. The highest energy cosmic rays seem to develop higher in the atmosphere, indicating a heavy composition, or at least not a pure proton one. Larger statistics or independent analysis of the fluctuations of $X_{\max}$ and SD mass composition estimators are needed to strengthen these results.

Photon induced showers have a strong individuality compared to the showers induced by nuclei. They develop slower in the atmosphere having a larger $X_{\max}$. The main reason is the smaller multiplicity in the electromagnetic interactions compared to the hadronic ones combined with the LPM effect. Photon showers also contain fewer secondary muons, which combined with the deep penetration in the atmosphere leads to large rise times of the signal in the SD tanks and to a shower front with a larger curvature than hadronic showers. These two parameters are combined into a single SD observable through the principal component analysis to maximize the discrimination power [14]. The Pierre Auger collaboration has derived a direct limit on the flux of photons for the first time by searching for photon candidates and relating their number to the exposure of the surface array. No photons have been found in the Auger data and therefore only limits on the photon fraction are shown in Fig. 4 (left). These limits improve significantly upon bounds from previous experiments, excluding some top down models as the super-heavy dark matter scenario. The flux expected for GZK photons will be reached with data accumulating

over the next years.

In the case of the topological defects models, the UHECRs sources are distributed all over the universe and most of the high energy photons interact with the cosmic microwave background. The photon flux at Earth would be low in this scenario while the neutrino flux is not attenuated. The upper limit on the diffuse flux of ultra high energy tau neutrinos, presented in Fig. 4 (right), was built based on the search for neutrinos with the characteristics of extremely inclined, deeply penetrating events with a large electromagnetic component [15]. The Pierre Auger Observatory is most sensitive to Earth-skimming ν_τ in the energy range where the GZK neutrinos are expected. The derived limit in the energy range $2 \cdot 10^{17}$- $2 \cdot 10^{19}$ eV is at present the most sensitive bound.

4 Conclusions

The southern Pierre Auger Observatory will be completed at the end of 2008. Already with a data set that is comparable to the statistics of one year fully operational array, the hypothesis of a continuation of the energy spectrum in the form of a power law above an energy of $10^{19.6}$ eV is rejected with 6 sigma significance. This result is independent of the energy scale uncertainties. Combined with the directional correlation of the highest energetic cosmic rays with nearby active galactic nuclei [16] the observed flux suppression suggests the existence of a GZK-effect. A mixed composition of the cosmic rays is present over the whole energy range and upper limits on photon and neutrino fluxes are given. The nature of the highest energies will be determined more precisely within the following year with increased statistics and different observables.

References

1. K. Greisen, *Phys. Rev. Lett.* **16**, 748 (1966).
2. G.T. Zatsepin and V.A. Kuz'min, *JETP Lett.* **4**, 78 (1966).
3. M. Roth [Pierre Auger Collaboration], *Proc. 30th ICRC, Mérida* (2007), arXiv:0706.2096v1 [astro-ph].
4. R.U. Abbasi *et al.*, *Phys. Rev. Lett.* **100**, 101101 (2008).
5. M. Takeda *et al.*, *Astropart. Phys.* **19**, 447 (2003).
6. J. Abraham *et al.* [Pierre Auger Collaboration], *Nucl. Instrum. Methods* A **523**, 50 (2004).
7. X. Bertou *et al.* [Pierre Auger Collaboration], *Nucl. Instrum. Methods* A **568**, 839 (2006).
8. M. Unger *et al.*, *Nucl. Instrum. Methods* A **588**, 433 (2008).
9. D. Allard [Pierre Auger Collaboration], *Proc. 29th ICRC, Pune* **7**, 287 (2005).
10. T. Yamamoto [Pierre Auger Collaboration], *Proc. 30th ICRC, Mérida* (2007), arXiv:0707.2638 [astro-ph].
11. P. Facal San Luis [Pierre Auger Collaboration], *Proc. 30th ICRC, Mérida* (2007), arXiv:0706.4322 [astro-ph].
12. L. Perrone [Pierre Auger Collaboration], *Proc. 30th ICRC, Mérida* (2007), arXiv:0706.2643 [astro-ph].
13. M. Unger [Pierre Auger Collaboration], *Proc. 30th ICRC, Mérida* (2007), arXiv:0706.1495v1 [astro-ph].
14. J. Abraham *et al.* [Pierre Auger Collaboration], *Astropart. Phys.* **29**, 243-256 (2008).
15. J. Abraham *et al.* [Pierre Auger Collaboration], *Phys. Rev. Lett.* **100**, 211101 (2008).
16. J. Abraham *et al.* [Pierre Auger Collaboration], *Astropart. Phys.* **29**, 188 (2008); J. Abraham *et al.* [Pierre Auger Collaboration], *Science* **318**, 939 (2007).

STUDY OF THE ULTRA HIGH ENERGY COSMIC RAYS ARRIVAL DIRECTIONS WITH THE PIERRE AUGER OBSERVATORY

R. BONINO for the Pierre Auger Collaboration
Istituto di Fisica dello Spazio Interplanetario (INAF), Università di Torino and Sezione INFN Torino, Italy

We present the first results about the studies of Ultra High Energy Cosmic Rays arrival directions using the early data collected at the Pierre Auger Observatory [1] (corresponding to $\sim$ 1 year of data taking of the complete southern array). We discuss in particular:

- the analysis of large-scale patterns in the arrival directions of cosmic rays;
- a search for an excess of events from the direction of the Galactic Center region and from some extragalactic objects;
- the observed correlation between cosmic rays with energies above 60 EeV (1 EeV = 10^{18} eV) and the directions of nearby active galactic nuclei (AGN).

1 Introduction

The identification of the sources of ultra-high energy cosmic rays and the comprehension of the mechanisms by which they acquire their energies have been great challenges since the detection of the first 10^{20} eV event in 1962 at Volcano Ranch [2].

The maximum energy attainable in an accelerator with characteristic magnetic field B and size L is of order $E_{max} \sim ZeBL$. Only a few types of astronomical objects appear able to accelerate protons to 10^{20} eV; these include Active Galactic Nuclei, galaxy clusters, and objects with large radio lobes.

Furthermore, particles with energies above about $6 \cdot 10^{19}$ eV are expected to interact inelastically with cosmic microwave background photons, losing energy at each interaction. As a consequence the cosmic ray flux may be significantly reduced above 100 EeV. Particles exceeding the interaction energy threshold and originating at distances greater than 100 Mpc should never be observed on Earth. This effect, known as the "GZK effect" [3,4], requires the sources of the cosmic rays observed at Earth to be relatively nearby, within about 100 Mpc at most, further reducing the number of possible candidates.

Among the observables that might help to solve the puzzle of the sources, one of the most effective is the study of anisotropy in the UHECR arrival directions. In air-shower experiments the incoming directions of the highest energy cosmic rays are determined well and hence it is possible to estimate whether or not they are isotropically distributed on the sky. At the highest energies ($> 5 \cdot 10^{19}$ eV) the arrival directions point back to the sources because these particles should be only slightly deflected by magnetic fields.

In anisotropy studies, especially on small angular scales, it is fundamental to determine the arrival direction of cosmic rays with great precision. Consequently, an accurate knowledge of

the angular resolution of the Auger Surface Detector (SD) is required. We discuss this in section 2, followed by a presentation of results on large- and small-scale anisotropy. The first specific targets chosen by the Auger Collaboration have been the Galactic Center at EeV energies and BL-Lacs and AGN at higher energies.

2 Angular resolution of the Surface Detector

The arrival direction of a SD event is determined by fitting the arrival time of the first particle in each station to a shower front model (see fig.1). The precision achieved in the arrival direction reconstruction depends therefore on the uncertainty in the time measurement and on the effectiveness of the shower front model adopted [5].

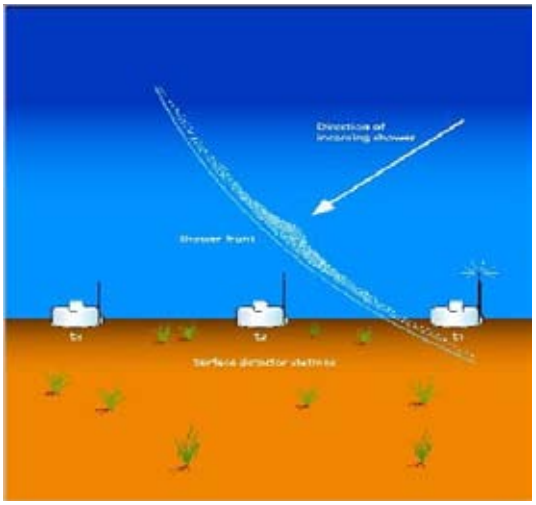

Figure 1: Sketch of the shower front arrival.

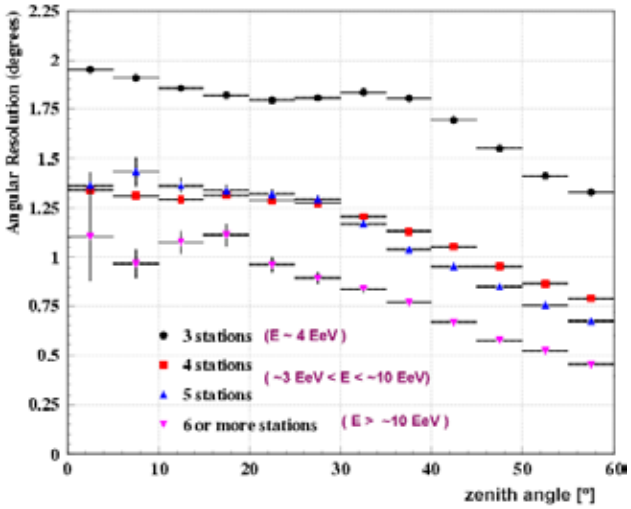

Figure 2: SD angular resolution as a function of zenith angle for different station multiplicities.

The angular resolution is calculated on an event by event basis, from the zenith (θ) and azimuth (ϕ) uncertainties of the geometrical reconstruction. It is defined as the angular radius that would contain 68% of showers coming from a point source.

In fig.2 the angular resolution is shown as a function of the zenith angles for various station multiplicities [6]. It is better than 2° in the worst case of vertical showers with only 3 stations hit and improves significantly with the number of stations. For events with 6 or more stations, corresponding to events with energies above 10 EeV, it is always better than 1°.

3 Large scale anisotropy studies

Lower energy cosmic rays likely originate within our Galaxy, while higher energy particles are believed to be extragalactic. At the transition the large scale angular distribution might change significantly. Large scale anisotropy, especially its evolution with primary energy, represents one of the main tools for discerning between the galactic and extragalactic origin of cosmic rays and for understanding their mechanisms of propagation.

If the transition to extra-galactic sources occurs at the ankle of the spectrum [7], then at 10^{18} eV cosmic rays are still mainly galactic and their diffusive escape from the Galaxy may be efficient enough so that the sky distribution of their arrival directions is not isotropic. The predictions for the shape and amplitude of the corresponding anisotropy are very model-dependent, but a %-level modulation is plausible [8].

On the other hand, if the transition occurs at lower energy [9], i.e. around $5 \cdot 10^{17}$ eV, then 10^{18} eV cosmic rays are already extragalactic and their sources may be cosmologically distributed. If

so then no large-scale pattern would be detectable except for the CMB-like dipole anisotropy[10]. In this case anisotropy amplitudes of the order of $\sim 0.6\%$ are expected.

3.1 Auger results

The statistics accumulated so far by the Auger Observatory permits the study of %-level large-scale patterns, but this is challenging due to the difficulty of controlling the sky exposure of the detector and various acceptance effects, such as detector instabilities and weather modulations.

In order to avoid such problems three complementary analyses have been performed. All show that at EeV energies the Right Ascension (RA) distribution is remarkably compatible with an isotropic sky; an upper limit on the first harmonic modulation of 1.4% in the energy range $1 < E < 3$ EeV has been set [11] (see fig.3 for more details). This result does not confirm the 4% RA modulation found by the AGASA experiment [12] (although the sky regions covered by the two experiments are different) and already sets some constraints on the galactic hypothesis (further statistics and analysis are in any case necessary).

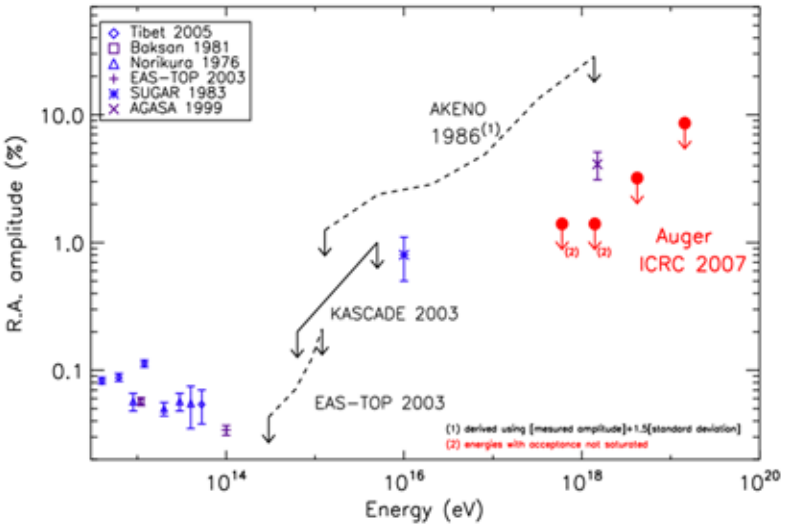

Figure 3: Overview on the results of large scale anisotropy studies; Auger upper limits are drawn *in red*.

4 The Galactic Center region

The Galactic Center is one of the most interesting targets in the study of small scale anisotropies at EeV energies because it contains a super massive black hole, a good candidate accelerator of high-energy cosmic rays. This black hole is believed to be associated with the radio emissions from Sagittarius A*. The H.E.S.S. collaboration has recently observed TeV γ-ray emissions close to this radio source [13]. A further reason of interest for this region is the privileged position of the Pierre Auger Observatory: the GC passes only 6° away from the observatory zenith.

In the past there have been claims of excesses of cosmic rays from the GC region from the AGASA [12] and SUGAR [14] experiments. Both the excesses are located in regions near the GC but not coincident with it (in the case of AGASA the GC is not in its field of view).

4.1 Auger results

Besides the privileged position, another advantage for Auger comes from the exposure of the array: the number of EeV cosmic rays accumulated so far from this part of the sky greatly exceeds that from previous experiments.

The claims of the forerunner experiments are periodically tested by the Auger experiment in different energy ranges and window sizes. In the most recent analysis two different energy ranges have been considered, 0.1-1 EeV and 1-10 EeV, but no significant flux excess has been found in the region around the GC (see tab.1: the numbers of observed events are always compatible with the expected ones) [15]. The distribution of Li-Ma significances for overdensities in this region is consistent with an isotropic sky for both energy ranges.

Table 1: Summary of excesses searches for $0.1 < E < 1$ EeV (*top*) and $1 < E < 10$ EeV (*bottom*) around the GC in the form of both extended and point-like source.

search	window size	n_{obs}/n_{exp}
extended	10° (TH)	5663 / 5657 = 1.00 ± 0.02(stat) ± 0.01(syst)
	20° (TH)	22274 / 22440 = 0.99 ± 0.01(stat) ± 0.01(syst)
point-like	1.3° (G)	192.1 / 191.2 = 1.00 ± 0.07(stat) ± 0.01(syst)

search	window size	n_{obs}/n_{exp}
extended	10° (TH)	1463 / 1365 = 1.07 ± 0.04(stat) ± 0.01(syst)
	20° (TH)	5559 / 5407 = 1.03 ± 0.02(stat) ± 0.01(syst)
point-like	0.8° (G)	16.9 / 17.0 = 0.99 ± 0.17(stat) ± 0.01(syst)

5 Correlation of UHECR with nearby extra-galactic objects

At the highest energies, above a few $\times 10^{19}$ eV, cosmic rays should be only slightly deflected by magnetic fields. A direct way to search for sources of UHECR is to analyze the distribution of their arrival directions for small-scale clustering and specifically to search for correlations with known astronomical objects that are candidate sources.

5.1 Active Galactic Nuclei

AGN have long been considered to be sites where energetic particle production might take place, and where protons and heavier nuclei could be accelerated up to the highest energies measured so far.

The Auger collaboration searched for a correlation of its highest energy events with these astronomical objects (the selected AGN come from the 12th edition of Véron-Cetty/Véron catalogue [16]). The data set analyzed has been acquired by the surface array during the first 3.5 years of data taking and corresponds to an integrated exposure of about 9000 km^2 sr yr.

Under the assumption of isotropy, it's possible to calculate the probability that any given cosmic ray falls within a fixed distance from any AGN, i.e. the probability P for a set of N events from an isotropic flux to contain k or more events at a maximum angular distance ψ from any member of a collection of candidate point sources. P is given by the cumulative binomial distribution $\sum_{j=k}^{N} C_j^N p^j (1-p)^{N-j}$, where p is the fraction of the sky (weighted by the exposure) defined by the regions at angular separation less than ψ from the selected sources. The degree of correlation has been computed as a function of three parameters: the maximum angular separations ψ_{max}, the maximum AGN distance D_{max} and energy thresholds E_{th}.

The strategy adopted in this analysis requires as a first step an exploratory scan for the minimum of P, aimed to identify the configuration of parameters that maximizes the correlation. The absolute minimum of P was found for $\psi_{max} = 3.1°$, $z_{max} = 0.018$ ($D_{max} = 75$ Mpc) and $E_{th} = 56$ EeV. In this optimized configuration 12 events among 15 correlated with the selected AGN, while only 3.2 were expected by chance if the flux were isotropic.

To avoid the negative impact of trial factors in *a posteriori* search, the Auger collaboration decided to test this hint of anisotropy on an independent data set with parameters specified *a priori*. A prescription was written down, fixing the set of parameters and sources; new data would be analyzed sequentially until the probability to incorrectly reject isotropy was 1% and the probability to incorrectly reject correlation was 5%.

This prescription was tested on an independent data set collected after 27 May 2006 (when the prescription started), with exactly the same reconstruction and calibration algorithms as in the exploratory scan. On 25 May 2007, 6 out of 8 events were found to fulfill the prescription.

After the successful result of this test, a re-scan of the full data set (from 1 January 2004 to 31 August 2007) was performed, adopting newer and somewhat more accurate reconstruction and calibration algorithms. A similar result is obtained, with the correlation maximized for the 27 events with energies above 57 EeV: 20 of these events correlate with at least one AGN for a maximum angular separation $\psi_{max} = 3.2°$ and a maximum distance to AGN $D_{max} \sim 71$ Mpc. The results of this analysis are shown in fig.4.

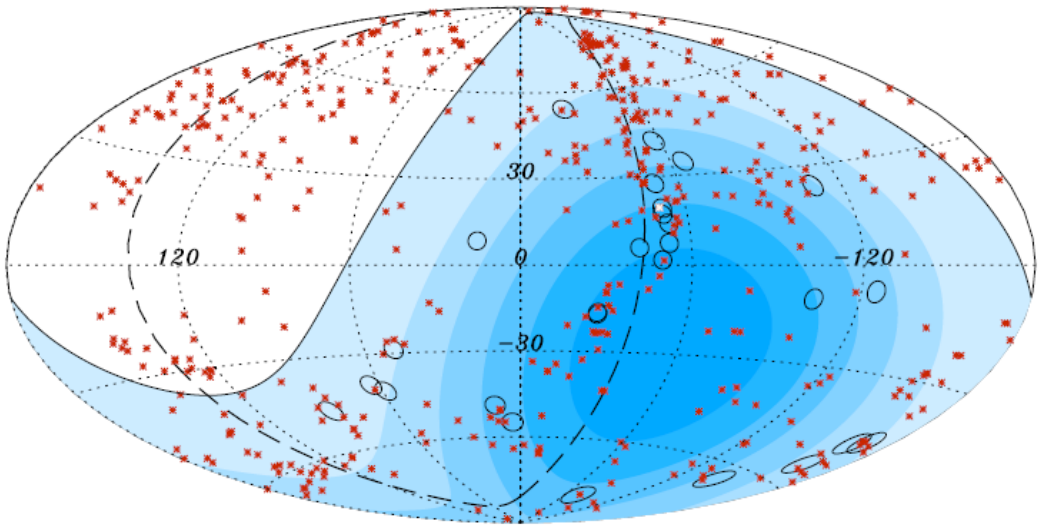

Figure 4: Projection on the celestial sphere in galactic coordinates with circles of radius 3.2° centered at the arrival directions of the 27 cosmic rays with highest energy detected by Auger. The positions of the selected 472 AGN are indicated by red asterisks.

Summarizing, the most important results of this analysis are:

- The anisotropy of UHECR (above 57 EeV) has been confirmed at 99% CL with an a priori test on an independent data set (in [17] a detailed report is given). This is the first time that a so strong signal of correlation is revealed and the hypothesis of an isotropic distribution of these cosmic rays is rejected at such a confidence level.

- The observed correlation is compatible with the hypothesis that UHECR originate from extra-galactic sources within the GZK horizon (i.e. compatible with the flux suppression observed in the spectrum starting at ~ 60 EeV [18]).

- The angular scale of the correlation is a few degrees, suggesting a predominantly light composition.

- AGN are the tracers but cannot be identified unambiguously as the sources: objects with a similar spatial distribution (GRB, quasar remnants, ...) are not excluded. It is also plausible that only a subclass of AGN are the sources.

- Several events lie close to the super-galactic plane (particularly close to Cen A) whereas a paucity of events has been recorded from Virgo.

The Véron-Cetty/Véron catalogue chosen for the correlation search is one of the largest collection of such objects but it is not an unbiased statistical sample. It is incomplete around the Galactic plane and for objects distances greater than 100 Mpc. It is important to note that these flaws are not an obstacle to the limited aim of demonstrating anisotropy.

A significant increase in ultra-high energy cosmic-ray statistics, combined with the future northern site of Auger, should lead to an unambiguous identification of the sources and their characteristics.

5.2 BL-Lacs

Active Galactic Nuclei include different sub-classes of astronomical objects. One of the more attractive candidate classes for UHECR sources is that of BL-Lacs. These are blazars in which the relativistic jet axis of the active galaxy is aligned with our line of sight.

Significant correlations of arrival directions of UHECR with positions of BL-Lacs were found by forerunner experiments with different subsets of BL Lacs and setting different energy thresholds.

A test on all these correlations has been performed with the present Auger data set which is already 6 times larger than those used in preceding cross-correlation searches for energies above 10 EeV. The results of this test [19] do not support previously reported excesses of correlation since the number of correlations found is compatible with that expected for an isotropic flux.

References

1. J.Abraham et al. [Pierre Auger Collaboration], *Nucl. Instrum. Methods* A **523**, 50 (2004).
2. J.Linsley, *Phys. Rev. Lett.* **10**, 146 (1963).
3. K.Greisen, *Phys. Rev. Lett.* **16**, 748 (1966).
4. G.T.Zatsepin and V.A.Kuz'min, *Sov. Phys. JETP Lett.* **4**, 78 (1966).
5. C.Bonifazi et al., *Astropart. Phys.* **28**, 523 (2008).
6. M.Ave [Pierre Auger Collaboration], *Proc. 30th ICRC, Mérida* (2007), arXiv:astro-ph/0709.2125.
7. M.A.Hillas, *J. Phys.* G **31** R95 (2005).
8. Candia et al., *J. Cosmol. Astropart. Phys.* **05**, 003 (2003).
9. V.Berezinsky et al., *Phys. Rev.* D **74**, 043005 (2006).
10. D.J.Schwarz et al., *Phys. Rev. Lett.* **93**, 221301 (2004)
11. E.Armengaud [Pierre Auger Collaboration], *Proc. 30th ICRC, Mérida* (2007), arXiv:astro-ph/0706.2640.
12. N.Hayashida et al., *Astropart. Phys.* **10**, 303 (1999).
13. F.Aharonian et al., *Astron.&Astrophys.* **425**, L13 (2004).
14. J.A.Bellido et al., *Astropart.Phys.* **15**, 167 (2001).
15. E.M.Santos [Pierre Auger Collaboration], *Proc. 30th ICRC, Mérida* (2007), arXiv:astro-ph/0706.2669.
16. M.-P. Véron-Cetty and P. Véron., *Astron.&Astrophys.* **455**, 773 (2006).
17. J.Abraham et al. [Pierre Auger Collaboration], *Science* **318**, 938 (2007); J.Abraham et al. [Pierre Auger Collaboration], *Astropart. Phys.* **29**, 188 (2008).
18. M.Roth [Pierre Auger Collaboration], *Proc. 30th ICRC, Mérida* (2007), arXiv:astro-ph/0706.2096.
19. D.Harari [Pierre Auger Collaboration], *Proc. 30th ICRC, Mérida* (2007), arXiv:astro-ph/0706.1715.

A COMMENT ON CATALOG SEARCHES

P. TINYAKOV
Service Physique Theorique CP225, Université Libre de Bruxelles,
Boulevard du Triomphe 1050 Bruxelles

We illustrate in a concrete example that a mere positional correlation of highest-energy cosmic rays with active galactic nuclei (AGN), although suggests, does not necessarily imply that the latter are sources of the cosmic rays. Different interpretations of this correlation are possible, and signatures other than positional correlations are needed to discriminate between them. We point out that some of these signatures seem to disfavor the AGN interpretation with already existing data.

In this talk I would like to clarify two points related to the correlations between the ultra-high energy comic rays (UHECR) and nearby active galactic nuclei (AGN) from the catalog [1], which were recently found by the Pierre Auger Observatory (PAO) [2,3].

1 Contrary to naive expectation, a correlation of cosmic rays with AGN (or any other objects) *does not* automatically imply that the latter are cosmic ray sources. This is not related to the significance of the correlation, but follows from the very nature of the statistical test performed to establish the correlation. In positional correlation analysis one compares the distribution of the data events over the sky with the *isotropic* distribution. If the two distributions are found to be incompatible, this means simply that the data are *not isotropic*. The actual sources should be identified by different methods.

To illustrate the relevance of this point consider a concrete example. The same set of cosmic ray events which correlate with AGN in the PAO analysis may be cross-correlated, by the same method, with just one object for which we take Cen A, an active galaxy in the direction of the Centaurus supercluster. Cen A is a radio-galaxy which is exceptionally close to us: the distance to Cen A is about 3.5 Mpc. It possesses jets and radio lobes, the usual attributes of a potential acceleration site.

There is an excess of events in the data in the direction of Cen A. The significance of the excess at a given angular scale δ can be characterized by the probability $P(\delta)$ that equal or larger excess occurs by chance as a result of a fluctuation in the uniform distribution. The smaller is the probability to obtain a given excess by chance, the more significant it is. This probability may be determined by

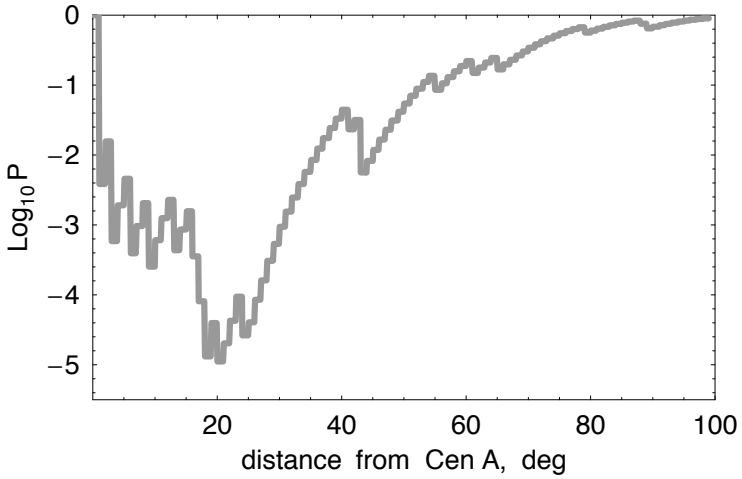

Figure 1: The probability P that the observed excess of events within angular distance δ around Cen A has occured by chance. The values of P are indicative only since their calculation accounts neither for the statistical penalty associated with the choice of angular scale nor for the bias in the sample.

the Monte-Carlo simulation. The result of the simulation is shown in Fig. 1. One can see that the excess is most significant at about 20°. Out of 27 events in total, 9 events fall within 20° from Cen A while only 1.5 are expected for the uniform distribution. Note that the events contributing to this correlation with Cen A are the same events that contribute to the correlation with AGN if the latter are assumed to be sources.

Such a situation is explained in the following way. The distribution of the nearby AGN is rather inhomogeneous. Moreover, Cen A is projected onto one of the largest nearby structures, the Centaurus supercluster, as can be seen on Fig.2. For this reason, the same data show correlations with both Cen A and AGN. Importantly, if either AGN or Cen A are indeed sources of highest-energy cosmic rays, *both* correlation signals will *increase* with the accumulation of statistics. So, a mere increase of significance will not allow to discriminate between the two possibilities.

2 It follows from the above that alternative signatures are needed to distinguish between the two cases. We present here one of such signatures.

The idea is that the cosmic ray flux predicted by the AGN hypothesis can be computed and compared to the observed one. In this way the AGN hypothesis itself will be subject to a test, not the hypothesis of the isotropic distribution.

The computation can be performed in a straightforward way taking into account the distance to AGN and the attenuation of protons of different energies (see Refs.[7,8] for details). The results are presented in Fig. 2 in the form of red crosses which show the positions of the nearby AGN. The intensity of a cross represents its expected contribution to the flux. This figure should be understood in a statistical sense: the fluxes of individual sources cannot, of course, be predicted without the detailed modeling of corresponding AGN (for which modeling there is probably not enough information anyway). However, in large groups of galaxies like galaxy clusters individual differences in luminosity will average away and only the common factors determined by the distance will remain. The relative contributions to the total flux from such groups can thus be reliably predicted.

One can observe the overdensity of the events in the direction of the Centaurus supercluster. The second region where a high flux is expected, the Virgo cluster, is completely devoid of events. This is a strange feature that does not look compatible with the AGN hypothesis.

The latter statement can be quantified by comparing the expected and observed distributions of events in the angular distance from the center of the Virgo cluster, as well as their distributions in Galactic and supergalactic longitudes and latitudes. The comparison may be performed by the Kolmogorov-Smirnov test. The results of different tests show different degree of incompatibility between the predicted and observed distributions with the probability that it has occured as a result of a

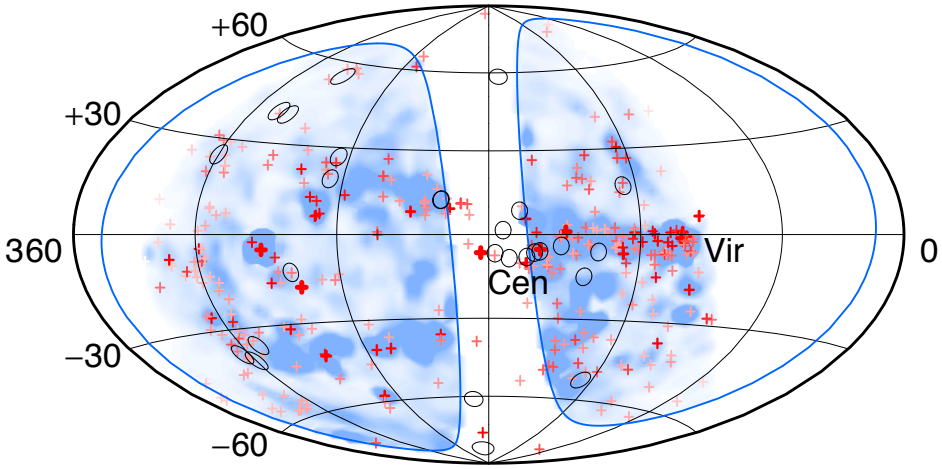

Figure 2: Hammer projection of the celestial sphere in supergalactic coordinates. Crosses show positions of nearby AGN. The color saturation of a given cross indicates the expected cosmic-ray flux with the account of the PAO exposure and the $1/r^2$ suppression, r being the distance to the source. Open circles represent 27 highest-energy cosmic rays detected by PAO. Shading shows the expected cosmic-ray flux from sources that follow the local matter distribution smoothed at the angular scale of 3.1° and convoluted with the PAO exposure (darker regions correspond to higher cosmic-ray flux). Blue lines cut out the region with Galactic latitude $|b| < 15°$ where the latter flux cannot be determined because of incompleteness of the source catalog. The positions of the Centaurus (Cen) and Virgo (Vir) superclusters are indicated.

fluctuation varying from 10% to 10^{-4}. Taking into account the strongest discrepancy and the number of tests performed, we estimate the significance of the tension between the AGN hypothesis and the data to be of order 99%.

One of the drawbacks of the analysis just described is the incompleteness of the AGN catalog. To check how much our results depend on this incompleteness we have replaced the catalog of AGN by a complete catalog of galaxies containing objects up to 270 Mpc [9]. The above tests performed with the AGN catalog replaced by the complete galaxy catalog show similar results. We think therefore that incompleteness of the catalog is not an issue.

Another drawback, which unfortunately cannot be avoided at present, is the *a posteriori* nature of the tests performed. To avoid this problem, the tests which we have described will have to be repeated with the new independent data. This is why now, before the new data arrive, it is particularly important to formulate other hypotheses and procedures to test them which may then be performed in a more reliable *a priori* way with independent data sets.

Acknowledgments

This work is supported in part by Belgian Science Policy under IUAP VI/11, by IISN and by the FNRS contract 1.5.335.08.

References

1. M.-P. Véron-Cetty and P. Véron. A catalogue of quasars and active nuclei: 12th edition. *Asrton. Astrophys.*, 455:773–777, August 2006.
2. J. Abraham et al. Correlation of the highest energy cosmic rays with nearby extragalactic objects. *Science*, 318:938–943, 2007.
3. J. Abraham et al. Correlation of the highest-energy cosmic rays with the positions of nearby active galactic nuclei. *Astropart. Phys.*, 29:188–204, 2008.
4. P. G. Tinyakov and I. I. Tkachev. Bl lacertae are sources of the observed ultra-high energy cosmic rays. *JETP Lett.*, 74:445–448, 2001.

5. P. G. Tinyakov and I. I. Tkachev. Cuts and penalties: Comment on 'clustering of ultrahigh energy cosmic rays and their sources'. *Phys. Rev.*, D69:128301, 2004.
6. Chad B. Finley and Stefan Westerhoff. On the evidence for clustering in the arrival directions of AGASA's ultrahigh energy cosmic rays. *Astropart. Phys.*, 21:359–367, 2004.
7. Dmitry Gorbunov, Peter Tinyakov, Igor Tkachev, and Sergey Troitsky. Comment on 'Correlation of the Highest-Energy Cosmic Rays with Nearby Extragalactic Objects'. 2007.
8. D. S. Gorbunov, P. G. Tinyakov, I. I. Tkachev, and S. V. Troitsky. On the interpretation of the cosmic-ray anisotropy at ultra-high energies. 2008.
9. O. E. Kalashev, B. A. Khrenov, P. Klimov, S. Sharakin, and Sergey V. Troitsky. Global anisotropy of arrival directions of ultra-high- energy cosmic rays: capabilities of space-based detectors. *JCAP*, 0803:003, 2008.